nature communications

Article | Article in Press

https://doi.org/10.1038/s41467-026-77787-4

Microglia and border-associated macrophages play opposite roles in cerebrovascular and leukocyte responses under systemic inflammation in male mice

Received: 7 May 2026

Accepted: 1 September 2026

Published online: 18 September 2026

Check for updates

Ana Rita Brás[1,2,11], Nikolett Lénárt[1,11], Damien Levard[3], Martina Glavan[3,10], Ákos Menyhárt[4,5], Csaba Cserép[1], Balázs Pósfai[1], Eszter Császár[1], Sai K. Reddy Samawar[6,7], Clare Pridans[8], Denis Vivien[3,9], Eszter Farkas[4,5], Lydia Sorokin[6,7], Marina Rubio[3] & Ádám Dénes[1]

Microglia closely associate with the vasculature, but their roles in leukocyte trafficking and cerebral blood flow (CBF) during systemic inflammation are unclear. We show that sustained systemic inflammation leads to altered microglia-vascular interactions, leukocyte recruitment to cerebral blood vessels and reduced hypercapnia-induced vasodilation. We find that microglia and border-associated macrophages (BAMs) play distinct roles in these processes: while BAM depletion with clodronate increases leukocyte recruitment, microglia/BAM depletion with PLX5622 and the absence of microglia but not BAMs in *CSF1R*$^{\Delta FIRE/\Delta FIRE}$ mice result in markedly reduced leukocyte recruitment. Supporting this, conditional microglial IL-1 deletion inhibits leukocyte recruitment. Unlike BAM depletion, the absence of microglia impairs hypercapnia-induced vasodilation, while in vivo two-photon imaging reveals microglial IL-1α-dependent interactions between leukocytes and penetrating arteries. Accordingly, reduced hypercapnia-induced vasodilation involves endothelial IL-1R1 and microglial IL-1α. Thus, distinct brain macrophage populations exert opposite effects on leukocyte recruitment and CBF through IL-1 dependent mechanisms in given vascular beds in male mice.

Myeloid cells in the CNS emerge as key regulators of brain homeostasis in addition to their roles in immune responses[1–4]. While microglia represent the main immune cell population of the CNS parenchyma, border-associated macrophages (BAMs) reside in the meningeal compartment (meningeal macrophages) or perivascularly (perivascular macrophages) across the brain[5,6]. Microglia establish direct interactions with all cell types of the neurovascular unit (NVU), and recent studies show a critical role of microglia in regulating vascular inflammation and dynamics from development to adulthood[7–13]. In particular, the highly dynamic microglial processes rapidly respond to changes in cerebral blood flow (CBF)[14], and microglia play an emerging role in shaping cerebral perfusion[8]. After acute brain injury or infection, blood-borne leukocytes contribute to vascular inflammation, blood-brain barrier (BBB) injury, and changes in CBF, while leukocyte recruitment is modulated by microglia, although the precise underlying mechanisms remain to be clarified[15,16].

While microglia markedly change their phenotype under systemic inflammatory conditions in both mice and humans[17–20], the modulation of inflammatory processes by microglia via interactions with different cell types of the NVU under inflammatory conditions is improperly

A full list of affiliations appears at the end of the paper. denes.adam@koki.hun-ren.hu

defined. Understanding these mechanisms would have strong clinical relevance, because chronic diseases and underlying systemic inflammation not only represent key risk factors for CNS disorders, but they are also frequently associated with altered leukocyte-vascular interactions, reduction of CBF and/or altered microglial activity even before clinical symptoms arise[21–24]. Microglia-vascular interactions are influenced by a broad array of cytokines, chemokines, and adhesion molecules[5,25]. Among these, interleukin-1 (IL-1), the key proinflammatory cytokine, is a central player in regulating immune responses, BBB integrity, and leukocyte recruitment into the brain[26–29]. At present, the regulation of leukocyte recruitment and CBF by microglia (a major source of IL-1) under systemic inflammatory conditions remains largely unclear, due to the limited number of studies where microglial function has been targeted. In line with this, the role of BAMs in neuroinflammatory processes is emerging, while studies targeting microglia and BAMs separately are limited. Here, we established a model of sustained systemic inflammation that results in recruitment of leukocytes to the brain, associated with impaired baseline CBF and hypercapnia-induced vasodilation response without any direct manipulation of the brain. By using microglia and BAM depletion, microglia, but not BAM-deficient CSF1R$^{\Delta FIRE/\Delta FIRE}$ mice, and conditional deletion of microglial IL-1 combined with inhibition of IL-1 signaling, we identify a distinct role for microglia and BAMs in leukocyte responses and CBF modulation. We also reveal a novel mechanism through which adhering intra-vascular leukocytes shape CBF responses specifically in arteries via microglial IL-1α, in line with the broad effects of IL-1 on leukocyte recruitment in different vascular beds.

Results

Sustained systemic inflammation results in leukocyte recruitment into the brain

Studies investigating leukocyte recruitment to the brain have used several mechanistically different approaches, including models of acute brain injury or inflammatory brain pathologies to date[16,30–34]. To study how leukocyte recruitment to the brain contributes to the detrimental vascular effects of inflammation and how this is influenced by microglial actions, we established a model of sustained systemic inflammation that leads to leukocyte recruitment without direct brain manipulation (Fig.1a, b and Fig. S1c, d). To this end, mice were treated with intraperitoneal (i.p.) LPS (E.coli, serotype O26:B6) for three consecutive days, resulting in moderate sickness behavior symptoms including piloerection, reduced locomotion, and rarely, diarrhea and fever with concomitant weight loss (Fig. S1a) as reported in the literature[35]. To visualize leukocytes in the brain, we used immunostaining against CD45, which is highly expressed on blood-borne cells, compared to microglia (Fig. S1b)[36–40]. Although some leukocytes were positive for Iba1, they were always negative for the microglial marker, P2Y12R (Fig. S1b right panel). Leukocyte recruitment affected several brain areas, including the cerebral cortex, striatum, thalamus, hypothalamus, and hippocampus (Fig. S1c). Recruited CD45$^+$ cells were quantified in the cortex and striatum, where a non-significant trend for increased cell numbers was apparent after the first LPS dose, with marked increases 24 h after the third LPS injection (Fig.1b and Fig. S1d). Making use of the combination of laminin α4 (expressed across the endothelial basement membrane (BM)[41,42]), aquaporin 4 (Aqp4) and glial fibrillary acidic protein (GFAP), the perivascular space was delineated, allowing the identification of leukocyte locations. Recruited leukocytes could be found beyond the astroglial BM, termed as transmigrated cells (Fig.1c I), while numerous intraluminal cells (Fig.1c III) and those attached to vessel walls or crossing blood vessels (Fig.1c II) were also observed (collectively termed as vessel-associated cells). A population of leukocytes was found to be trapped in the perivascular space (Fig.1d). In order to avoid incorporation of any bias to our CD45 quantifications, these perivascularly located CD45$^+$ cells were clearly distinguished from Lyve1$^+$ perivascular macrophages (PVMs) and from parenchymal Iba1$^+$ microglia by their distinct morphology and CD45 fluorescence intensity (Fig. S1e, f). Only 14% of leukocytes were double positive for CD45 and Iba1. We found that 90% of leukocytes remained vessel-associated, while 10% of the cells were found in the parenchyma (Fig.1e). To investigate the distribution of leukocytes along the vascular tree, we employed immunostaining for α-smooth muscle actin (SMA, to visualize arteries) and laminin α2 (lower level of expression in arteries compared to veins) to distinguish between the arterial and venous circulation[42,43] (Fig.1f, g). We first confirmed the co-localization of SMA with laminin α1– specific for meningeal and astroglial BM, expressed at higher levels in arterial than in venous segments (Fig.1f). Capillaries were further distinguished from postcapillary venules based on diameter and the intensity of laminin α2 staining (Fig. 1g), which was higher on the venous side[42–44]. Leukocyte transmigration has previously been reported to take place at the level of postcapillary venules[30,45]. Surprisingly, our quantifications revealed significantly more vessel-associated CD45$^+$ cells in the arterial compared to the venous compartment (Fig.1g), suggesting that these cells might be involved in CBF changes characteristic of systemic inflammation[46,47]. To understand central vascular effects of systemic inflammation, we first assessed vascular activation in vivo by molecular magnetic resonance imaging (MRI) combined with micro-sized particles of iron oxide (MPIOs) targeting VCAM-1, as reported earlier[48]. MRI revealed a non-significant trend for VCAM-1 upregulation (252% compared to saline) already after the first dose of LPS and a significant increase (487%) 24 h after the third injection. Accordingly, no gadolinium signal (white voxels) was detected in the brain parenchyma, showing a lack of evident BBB disruption (Fig.1h). To detect any nonspecific signal and potential BBB leakage, the experiment was repeated with IgG-conjugated MPIOs administered to a separate set of animals. Only a nonspecific signal primarily localized to the choroid plexus, ventricles, and occasionally along larger penetrating arteries, was found in line with previous literature data[49]. As no specific signal was detected in the parenchyma, further quantification was not performed (Fig. S1g). In contrast, VCAM-1-targeted MPIOs showed a widespread signal across the brain (Fig.1h), suggesting extensive vascular activation in the absence of IgG leakage (Fig. S1g). Supporting MRI data, no significant change in endothelial zonula occludens-1 (ZO-1) expression was detected based on fluorescence intensity quantifications, indicating maintained endothelial barrier function (Fig. S1h). However, development of vascular inflammation was indicated by ICAM-1 (Fig.1i) and lipocalin 2 (Lcn2[50], immunopositivity. Although a few non-vascular cells in saline animals were also stained for Lcn2, its endothelial staining was substantially increased due to LPS treatment (Fig. S1i, j), as also reported by others[51,52]. Flow cytometry analysis identified the majority of recruited cells as neutrophils (73%, CX3CR1^{low}, CD11b^{hi}, Ly6G^{hi} cells) with substantial contribution from CX3CR1$^+$ monocytes (13.5%, CX3CR1$^+$ CD11b^{hi}, Ly6C$^{int\text{-}hi}$ cells, Fig.1j and Fig. S1k), while T cells and B cells were represented as less than 4% of the total CD45$^+$ population (data not shown). A combined CD45 and Sjc4 immunostaining (a neutrophil-specific antibody clone[53–55]) corroborated this finding, revealing 73% double-positive neutrophils out of all CD45+ leukocytes (Fig. S1l). We also identified CCR2$^+$CX3CR1^{dim}CD45$^+$MPO$^-$ monocytes in immunostaining (Fig1kII-III). Neutrophils (Fig. 1kI), CX3CR1$^{gfp/+}$-monocytes (Fig.1l, white arrowheads), and CX3CR1$^-$ leukocytes (Fig.1l, yellow arrowheads) were all negative for P2Y12R, clearly distinguishing them from resident microglia (Fig.1l and Fig. S1b right panel).

Microglial interactions within the NVU are markedly altered upon sustained systemic inflammation

High resolution confocal laser-scanning microscopy (CLSM) revealed close interactions between microglia and the cerebral vasculature (Fig. S2a), including those between microglial processes and endothelial (laminin α4) or astroglial (laminin α2) BMs (Fig. S2b),

https://doi.org/10.1038/s41467-026-77787-4

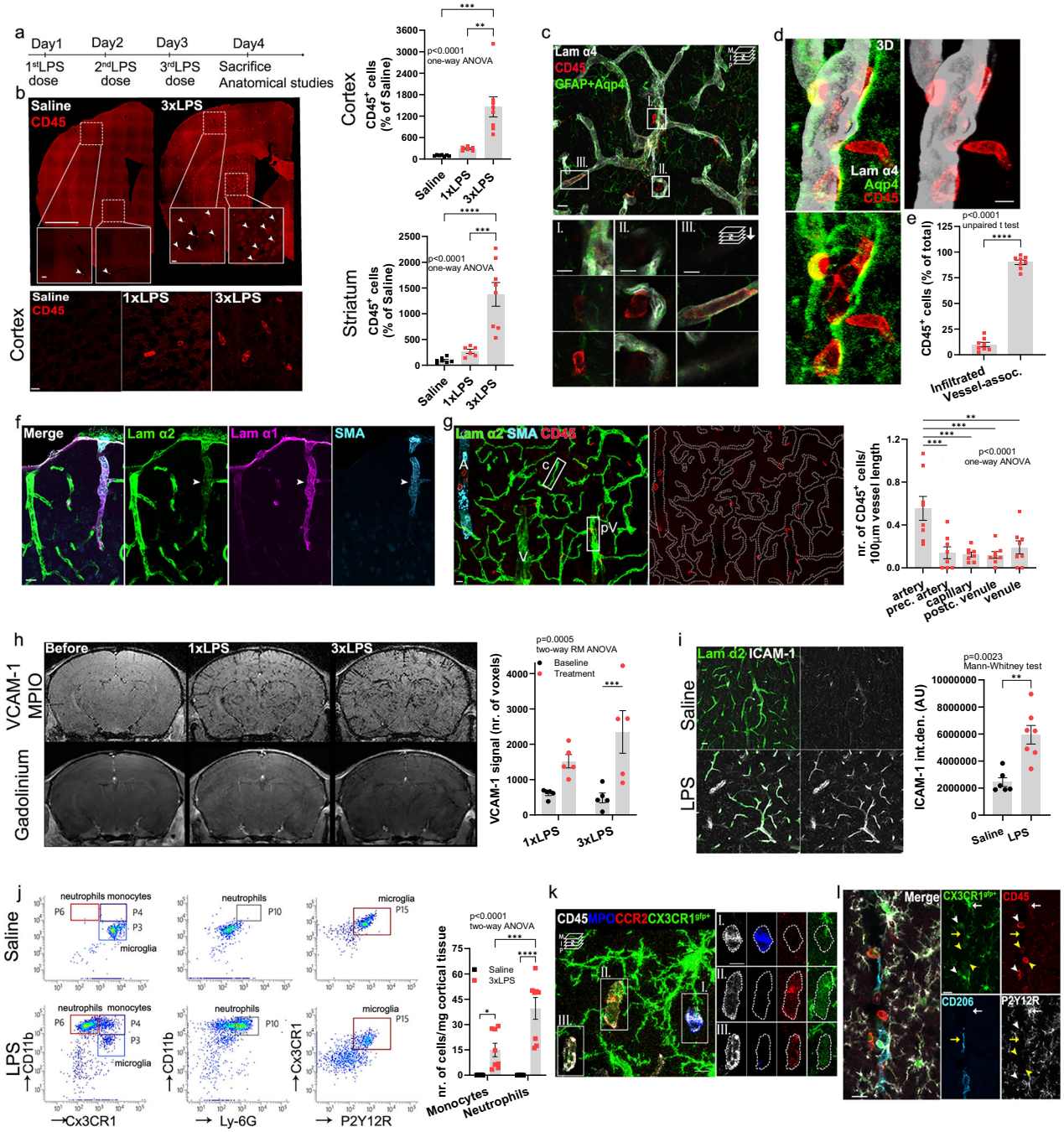

Fig. 1 | Sustained systemic inflammation results in leukocyte recruitment into the brain. a Experimental protocol. **b** Recruitment of CD45+ leukocytes in the cortex and striatum, $N = 7$ saline, $N = 6$ 1xLPS and $N = 8$ 3xLPS mice. pCortex<0.0001 one-way ANOVA, $p = 0.0001$ Saline vs 3xLPS, $p = 0.0011$ 1xLPS vs 3xLPS; pStriatum<0.0001, one-way ANOVA, $p < 0.0001$ Saline vs 3xLPS, $p = 0.0003$ 1xLPS vs 3xLPS. **c** Maximum intensity projection (MIP) from the cortex of a 3xLPS animal presenting: (I) transmigrated, (II) crossing or (III) intra-vascular leukocytes. **d** 3D reconstruction showing leukocyte localization with the endothelial BM (laminin α4) and the astroglial layer (Aqp4). **e** Transmigrated and vessel-associated $CD45^+$ cells. $N = 8$ mice per group, $p < 0.0001$ two-tailed unpaired *t*test. **f** Colocalization of α-SMA and laminin α1(arrowhead) in arteries. **g** Identification of vessels using laminin α2 and α-SMA. Arteriole-A, capillary-c, postcapillary venule-pV and venule-V. Quantification of $CD45^+$ cells after 3xLPS, N = 8 mice per group, $p < 0.0001$ one-way ANOVA, $p = 0.0006$ artery vs. precap. artery, $p = 0.0003$ artery vs capillary, $p < 0.0003$ artery vs postc. venule, p artery vs venule=0.0027. **h** Molecular MRI using VCAM-1-targeted MPIOs. Top panels VCAM-1 (dark voxels), bottom panels gadolinium signals (white voxels), $N = 5$ mice per group. $p = 0.0005$, two-way repeated measures ANOVA, $p = 0.0009$ Baseline vs 3xLPS. **i** Quantification of ICAM-1 signal (Integrated density, AU), $N = 6$ Saline and $N = 7$ 3xLPS mice, $p = 0.0023$ two-tailed Mann-Whitney test Saline vs 3xLPS. j) Recruited leukocytes analyzed by flow cytometry, $N = 5$ Control and $N = 9$ LPS mice. Gating: neutrophil: $CX3CR1^{low}CD11b^{hi}Ly\text{-}6G^{hi}$; monocytes: $CX3CR1^{int}CD11b^{hi}Ly6C^{int}$, microglia: $CX3CR1^{int}CD11b^{int}P2Y12^{hi}$, $p < 0.0001$ two-way ANOVA, $p = 0.0427$ Saline vs LPS monocytes, $p < 0.0001$ Saline vs LPS neutrophils, and $p = 0.0005$ 3xLPS monocytes vs 3xLPS neutrophils. **k** Representative CLSM MIP of neutrophils (I, $CX3CR1^{-}CCR2^{-}CD45^{+}MPO^{+}$) and monocytes (II $CD45^{+}CCR2^{+}CX3CR1^{int}MPO^{-}$ and III $CD45^{+}CCR2^{+}CX3CR1^{low}$ MPO^{-}). **l** Discrimination of microglia and PVMs from recruited $CD45^+$ leukocytes in $CX3CR1^{gfp/+}$ mice: $CX3CR1^{+}$ $P2Y12R^{+}$ $CD206^{-}$ $CD45^{lo\text{-}int}$ microglia (white arrow), $CX3CR1^{-}$ $P2Y12R^{-}$ $CD206^{+}$ $CD45^{-}$ PVMs (yellow arrow), and $CD45^{hi}$ $P2Y12R^{-}$ $CX3CR1^{+}$ (white arrowheads) or $CX3CR1^{-}$ monocytes (yellow arrowheads). Data presented as mean ± SEM: **b**,**e**,**g**–**j**; Sidak's multiple comparisons test: **a** Tukey's multiple comparisons test: **g** uncorrected Fisher's LSD: **h**,**j**; Scale bars: **b** 100 µm, inserts 10 µm, bottom row 10 µm; **c** 15 µm, inserts 5 µm; **d** 15 µm; **f**,**g** 20 µm; **i** 30 µm; **k**,**l** 15 µm all. Source data are provided as a Source Data file.

https://doi.org/10.1038/s41467-026-77787-4

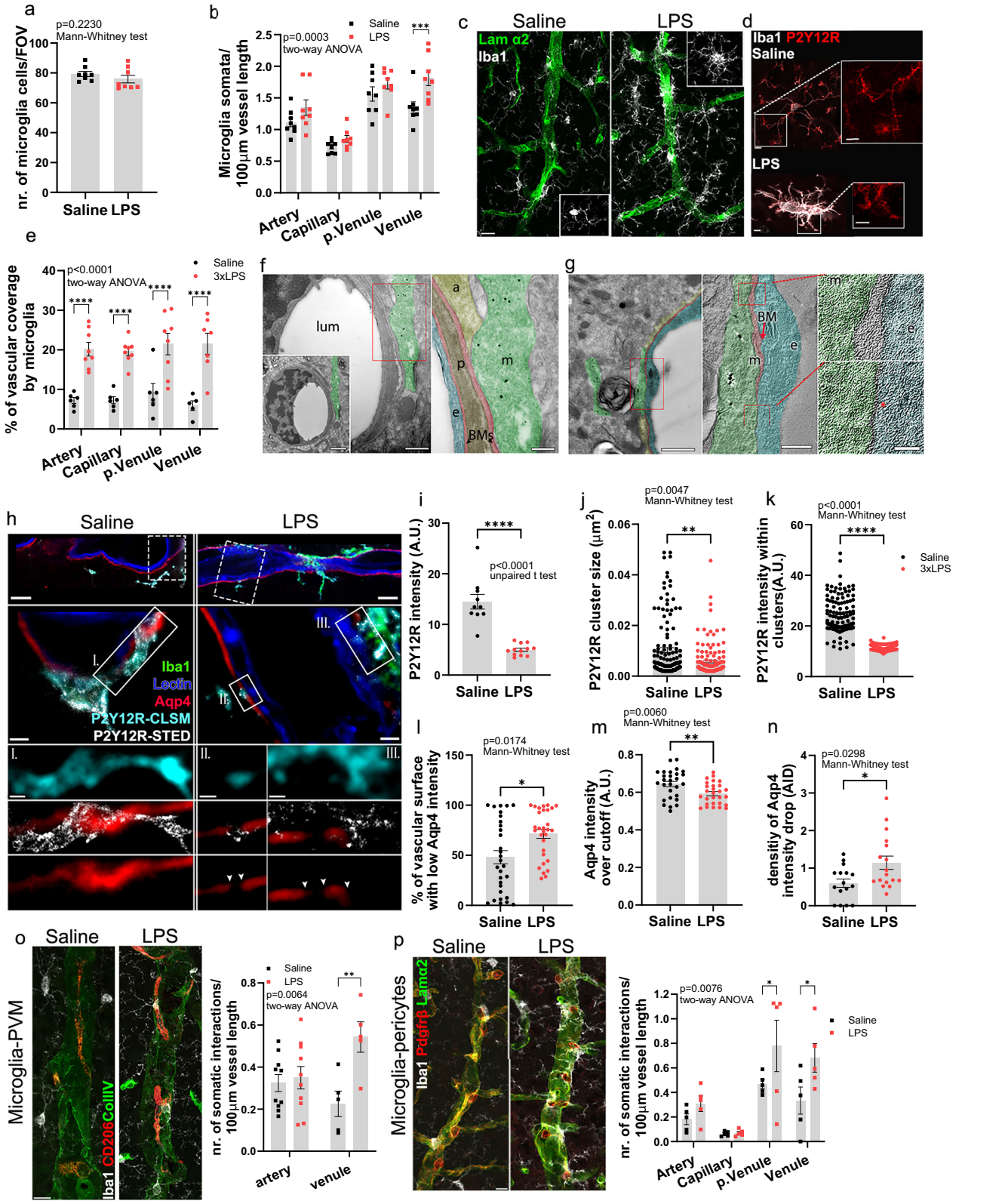

supporting our earlier findings[8]. Overall microglial numbers did not change in response to sustained systemic inflammation (Fig.2a). However, microglial somatic contact density increased on vessels, preferentially around venules (Fig.2b, c) and showed clear phenotypic changes (Fig.2c, d), resulting in increased vascular-microglial coverage in all vascular beds (Fig.2e). Microglial phenotype changes were most apparent after the 3rd LPS injection (Fig. S2c) in agreement with other studies[37,56]. Confirming our earlier findings[8], transmission electron tomography with Iba1-immunogold labeling revealed direct microglial membrane contacts with the vascular endothelium (Fig.2g) in the absence of systemic inflammation. We also identified indirect microglia-vessel contacts (Fig.2f), where astrocytic BM and pericytes are located between endothelial cells and microglial processes. To study this in a quantitative manner, we visualized microglial P2Y12Rs

Fig. 2 | Sustained systemic inflammation changes microglia-vascular interactions and disrupts astrocytic endfeet coverage of the vasculature. a Number of microglia in cortex, $N = 8$ mice per group, $p = 0.2230$ two-tailed Mann-Whitney test. **b** Distribution of microglial somata at given vascular segments, $N = 8$ mice per group, $p = 0.003$ two-way ANOVA, $p = 0.0006$ Saline vs LPS venule. **c** Recruitment of microglia to blood vessels and **d** microglial morphology changes after 3xLPS. **e** Microglial coverage along the vasculature, $N = 8$ mice per group, $p < 0.0001$ two-way ANOVA, $p < 0.0001$ Saline vs LPS artery, $p < 0.0001$ Saline vs LPS capillary, $p < 0.0001$ Saline vs LPS pVenule, $p < 0.0001$ Saline vs LPS venule. **f** Indirect and **g** direct microglia-endothelial interactions (*) by electron tomography in the S1 cortex from a saline mouse, Lum-lumen, p-pericyte (brown), a-astrocyte(yellow), e-endothelium (blue), BMs-basement membranes (red), m-microglia (green). **h** STED analysis on direct microglial process (P2Y12R, Iba1) -endothelial (Lectin) interaction sites void of Aqp4 staining in Saline vs LPS treated mice. Arrowheads: disruptions in Aqp4 staining referred to as AID (panel II. and III.), $N = 2$ mice per group quantificatified in (**i**–**n**). **i** P2Y12R signal intensity on individual microglial processes, $N = 10$ Saline and $N = 12$ LPS FOVs, $p < 0.0001$, two-tailed unpaired *t*test. **j** P2Y12R cluster size, $N = 137$ clusters, $p = 0.0047$, two-tailed Mann-Whitney test. **k** Signal intensity of P2Y12Rs within clusters, $N = 137$ clusters, $p < 0.0001$, two-tailed Mann-Whitney test. **l** Percentage of vascular surface area with low Aqp4 intensity, $N = 30$ FOVs, $p = 0.0174$, two-tailed Mann-Whitney test. **m** Number of high Aqp4 intensity values, $N = 28$ FOVs, $p = 0.0060$, two-tailed Mann-Whitney test. **n** Density of abrupt drop in Aqp4 signal intensity (AID), $N = 16$ Saline and $N = 17$ LPS FOVs, $p = 0.0298$, two-tailed Mann-Whitney test. o Somatic microglia-PVM interactions, $N = 5$ mice per group, $p = 0.0064$ two-way ANOVA followed by uncorrected Fisher's LSD test: $p = 0.0024$ Saline vs LPS venule. **p** Somatic microglia-pericyte interactions, $N = 5$ mice per group, $p = 0.0076$ two-way ANOVA followed by Tukey's multiple comparisons test: $p = 0.0323$ Saline vs LPS pVenule, $p = 0.0176$ Saline vs LPS venule; Data are presented as mean ± SEM: **a**,**b**,**c**,**i**,**j**,**k**,**l**,**m**,**n**,**o**,**p**; Sidak's multiple comparisons test: **b**,**e**; Scale bars: **c** 15 μm; **d** 5 μm all; **f** from left to right 2 μm, 1 μm, 400 nm; **g** from left to right 1 μm, 100 nm, 20 nm; **h** upper row 4 μm; second row 1 μm; inserts I–III 500 nm; o,p 5 μm. Source data are provided as a Source Data file.

that are functionally involved in microglia-vascular interactions[7,8], and the effects of systemic inflammation on microglial P2Y12Rs were assessed by combined CLSM/STED-super resolution nanoscopy (Fig.2h). We defined receptor clusters on our nanoscopy images as continuous areas of high-intensity labeling on the microglial surface by thresholding (see Methods). We found that P2Y12R intensity on microglial processes contacting vessels was significantly decreased in LPS-treated animals (Fig.2i), while the density of P2Y12R-clusters did not change (Fig. S2d). However, a significant reduction in cluster size (Fig.2j) and P2Y12R intensity within clusters (Fig.2k) was detected, suggesting that microglial P2Y12R expression is reduced due to systemic inflammation. We have previously shown that microglia directly contact endothelial cells via P2Y12R-mediated actions at sites lacking astroglial coverage[8]. Accordingly, we found that LPS-treated mice had significantly lower Aqp4 expression, as quantified by low (Fig.2l) and high (Fig.2m) Aqp4 fluorescent intensity values. In parallel, the density of abrupt intensity drops (AID) in the Aqp4 coverage of vessels was significantly higher (Fig.2h, n) in response to systemic inflammation, suggesting an altered vascular coverage by Aqp4$^+$ astrocytic endfeet. Damage to Aqp4$^+$ astrocytic endfeet in advanced systemic inflammation and increased permeability of the BBB for small molecules (10 kDa) were reported by others[18]. While in our experiments the lack of evident BBB leakage for the small gadolinium molecule (0.7 kDa, Fig.1h) and IgG-MPIOs (Fig. S1g) does not indicate major changes in BBB permeability on the endothelial side, detachment of Aqp4$^+$ astrocytic endfeet from blood vessels occurs in several CNS diseases and can be indicative of BBB dysfunction[57–59]. The presence of Aqp4 AIDs also frequently coincided with the presence of direct microglial process - endothelial contact sites (Fig.2h), suggesting that microglial processes may have access to endothelial cells at sites devoid of Aqp4+ astrocyte endfeet. In line with this, we found that somatic microglial contacts either with PVMs or pericytes, which were also apparent in the normal brain, increased along the venous, but not at the arterial segments (Fig.2o, p) under sustained systemic inflammation. This may indicate that crosstalk between BAMs and microglia under inflammatory conditions could contribute to leukocyte recruitment at the venous side and that other mechanisms than microglia-PVM or microglia-pericyte interactions may contribute to changes in arterial responses (e.g., regulation of CBF) in this experimental model.

Microglia and BAMs promote and hinder leukocyte recruitment into the brain parenchyma, respectively

Microglia produce chemokines to recruit leukocytes, while microglial phagocytosis also controls the number of infiltrating cells, as reported in different experimental models[15,16,60,61]. At present, the contribution of these opposing processes to leukocyte recruitment under systemic inflammation and the differential roles of microglia and BAMs are unclear. We found that microglia closely interact with transmigrated CD45$^+$ leukocytes (detected beyond the laminin α2$^+$ astroglial BM) in all vascular beds (Fig. 3a). To investigate the role of microglia in the recruitment of leukocytes under systemic inflammatory conditions, microglia were depleted from the brain by PLX5622 (Fig. S2f, h). Mice were fed a PLX5622 diet for 21 days, and LPS injections started on day 17, to assess leukocyte responses on day 21 after 3xLPS. We found significantly fewer recruited CD45$^+$ cells in microglia-depleted animals compared to controls (Fig.3b). The three weeks of PLX5622 treatment did not induce leukocyte recruitment to the brain, which was also verified in PLX5622 + saline-treated mice (Fig. S2e). In addition, previous flow cytometry analysis showed preserved peripheral immune cell populations in the liver, spleen, and blood after the application of this regimen[3,62,63], confirming that central recruitment of CD45$^+$ leukocytes was specifically attributed to systemic inflammation in this model, which was reduced in the absence of microglia. A non-significant trend for reduced vascular activation after microglia depletion was also seen based on ICAM-1 immunofluorescence (Fig. S2f, g). As PLX5622 depletes both microglia and BAMs (Figure. S2e, f, h, i), to dissect the specific role of microglia and BAMs in leukocyte recruitment, BAMs were selectively depleted using clodronate liposomes injected into the cisterna magna (i.c.m.)[64,65]. Clodronate is phagocytosed by CNS macrophages and leads to their apoptosis without affecting peripheral monocyte/macrophage and dendritic cell populations[64,66]. Effective depletion of BAMs without affecting microglia or other peripheral cell populations was confirmed by flow cytometry (S3b, c-g). For BAM depletion, LPS treatment started 5 days after i.c.m. Clodronate administration (referred to as day -5) (Fig.3c) as described earlier[64,65]. Importantly, selective BAM depletion showed the opposite effect to microglia depletion, recruiting more CD45$^+$ cells to the brain compared to controls (Fig.3d). To assess whether clodronate treatment affects vascular activation or BBB integrity, molecular MRI was performed using VCAM-1 or IgG-conjugated MPIOs. We found that clodronate treatment did not induce BBB disruption, as no parenchymal IgG leakage was detected, nor did it alter VCAM-1 expression (Fig. S3a). Five days after injection, clodronate efficiently depleted BAMs (Fig. S2j), as previously reported[64,65,67], without affecting other peripheral immune cell populations (Fig. S3c–e). However, by the end of LPS treatment (clodronate day -5 + LPS), the number of BAMs (CD206$^+$ cells) reached 40% of BAM numbers seen in controls (Fig. S2k), yielding only 60% depletion efficacy, which was also verified by flow cytometry (Fig. S3f). This increase in BAMs is likely to be an effect of prolonged systemic inflammation that may induce PVM repopulation, as reported earlier[68,69]. To avoid possible confounding effects of systemic inflammation on BAMs, we started the LPS treatment 24 h after clodronate injection (clodronate day 0 + LPS). Using this shorter protocol (Fig.3e), a significant increase

https://doi.org/10.1038/s41467-026-77787-4

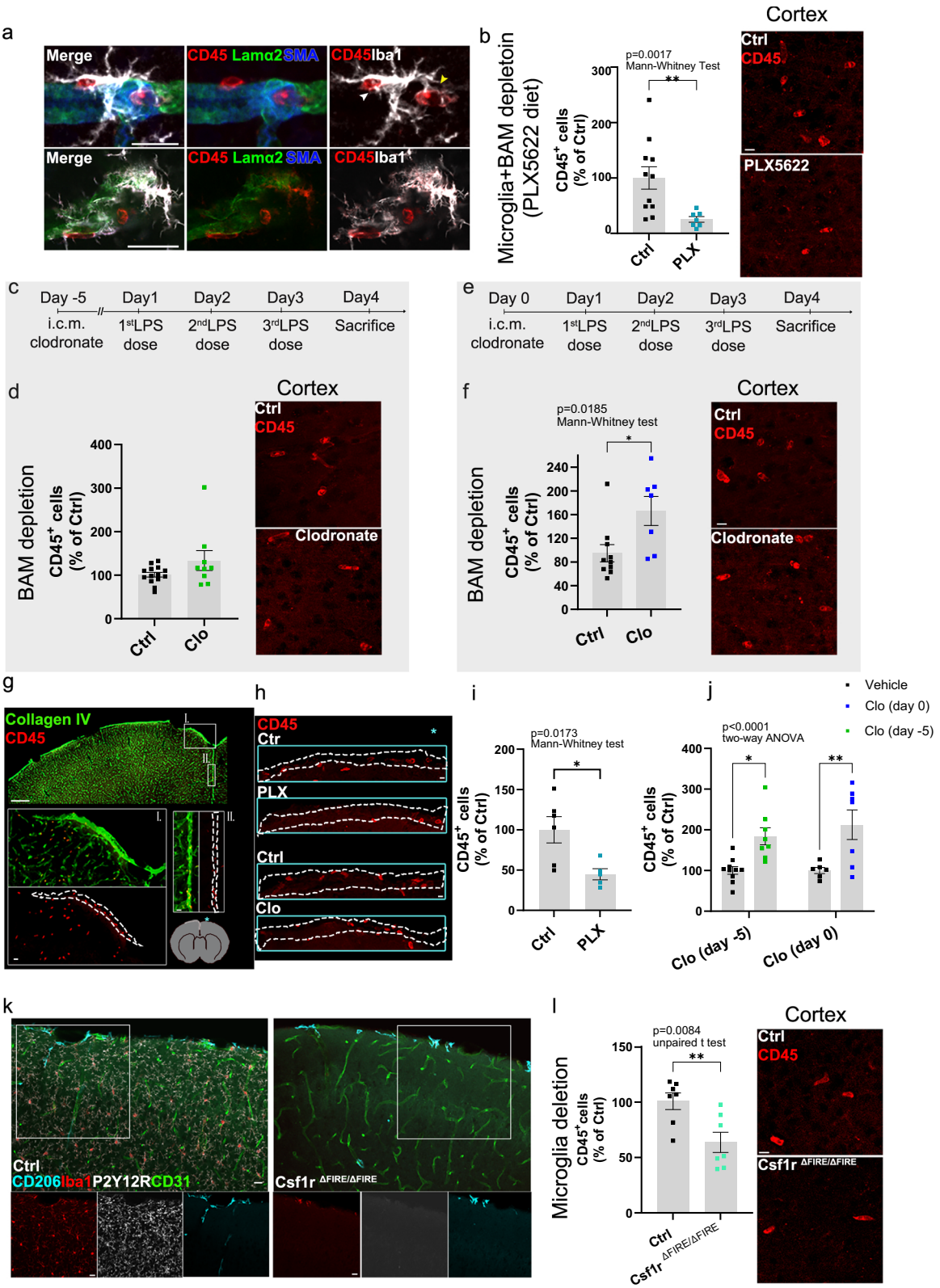

in leukocyte recruitment was seen in the cerebral cortex after BAM depletion (Fig.3f), and the overall BAM depletion rate by the end of the experiment reached 74% (Fig. S2l) without affecting microglia (Fig. S2m and Fig. S3g). As a separate population of BAMs is located in the meninges (meningeal macrophages), we also tested whether depletion by PLX5622 or clodronate has a different effect on leukocyte recruitment in the meninges (Fig.3g–j) during systemic inflammation. Supporting our findings above, the absence of microglia reduced (Fig.3h–i), while depletion of BAMs by clodronate increased the number of leukocytes in the meninges (Fig.3h, j) independent of the timing of clodronate administration. To further dissect the role of microglia and BAMs on leukocyte recruitment, we induced systemic

Fig. 3 | Microglia and BAMs play opposite roles in modulating leukocyte recruitment. a Microglia-leukocyte interactions at the vessel interface. **b** Leukocyte recruitment in the cortex of microglia+BAM depleted (PLX) animals $N = 11$ Control and $N = 7$ PLX mice, $p = 0.0017$, two-tailed Mann-Whitney test. **c** Experimental protocol for BAM depletion by intra-cisterna magna (i.c.m.) clodronate injection 5 days before LPS treatment (clodronate day -5). **d** Quantification of leukocytes in the cortex of BAM depleted (clodronate day -5) animals. $N = 14$ Control and $N = 9$ clodronate mice, $p = 0.206$ two-tailed Mann-Whitney test. **e** Experimental setting for BAM depletion by i.c.m. clodronate injection 24 h before the LPS treatment (clodronate day 0). **f** Quantification of leukocytes in the cortex of BAM depleted animals (clodronate day 0), $N = 10$ Control and $N = 7$ clodronate mice. $p = 0.0185$, two-tailed Mann-Whitney test. **g** Leukocyte recruitment in the meninges from the region above the cingular cortex and precentral area. **h** Leukocytes in the outlined region of the meninges marked with a cyan asterisk on panel g. **i** Leukocyte numbers in the meninges, $N = 6$ Control and $N = 5$ PLX5622 mice, $p = 0.0173$, two-tailed Mann-Whitney test. **j** Leukocyte counts in the meninges, $N = 10$ Control and $N = 8$ clodronate (day -5), $N = 6$ Control and $N = 7$ clodronate (day 0) mice, $p < 0.0001$ two-way ANOVA. **k** CLSM images of Control vs $CSF1R^{\Delta FIRE/\Delta FIRE}$ mice. **l** Quantification of leukocytes in the parenchyma of $CSF1R^{\Delta FIRE/\Delta FIRE}$ animals, $N = 7$ mice in both Control and $CSF1R^{\Delta FIRE/\Delta FIRE}$ groups, $p = 0.0048$ two-tailed unpaired *t*test. Data are presented as mean ± SEM: **b**,**d**,**f**,**i**,**j**,**l**; Scale bars: **a** 15 μm both panels; **b**,**e**,**f**,**h**,**l** 10 μm; **g** 200 μm, inserts 30 μm; **k** 20 μm all. Source data are provided as a Source Data file.

inflammation by 3xLPS in $CSF1R^{\Delta FIRE/\Delta FIRE}$ mice that lack microglia in the brain, while retaining BAM populations (Fig.3k)[70,71]. $CSF1R^{\Delta FIRE/\Delta FIRE}$ animals recapitulated the results of microglia depletion by PLX5622 in the brain parenchyma, having a significant reduction in recruited $CD45^+$ cells compared to control mice (Fig.3l). Within the meningeal compartment, $CSF1R^{\Delta FIRE/\Delta FIRE}$ mice showed a non-significant trend toward increased $CD45^+$ cell numbers relative to controls (Fig. S2n). Overall, these results suggest that in the context of systemic inflammation, microglia promote the recruitment of blood-borne peripheral leukocytes to the CNS, while BAMs limit it; this process was found to be independent of microglial P2Y12R (Fig. S3h).

Microglia promote leukocyte recruitment via IL-1β, IL-1α and IL-1R1 independently of endothelial IL-1R1 signaling

To study the mechanisms of leukocyte recruitment, we first tested the contribution of IL-1, the key proinflammatory cytokine involved in vascular inflammation and leukocyte recruitment[72,73]. After verifying the specificity of anti-IL-1α and anti-IL-1β antibodies on IL-1α/β KO tissues (Fig. S2o), we found microglial expression of both IL-1 isoforms in the 3xLPS model, while BAMs ($CD206^+$ $P2Y12R^-$ cells) were consistently negative for IL-1 (Fig.4a, b). To clarify the contribution of microglia-derived IL-1 to leukocyte recruitment, we generated transgenic mice conditionally deleted either for microglial IL-1α or for IL-1β ($IL\text{-}1\alpha^{fl/fl\Delta CX3CR1}$ or $IL\text{-}1\beta^{fl/fl\Delta CX3CR1}$ mice, respectively). Our results showed a significant, close to 50% decrease in leukocyte numbers in the cortex of both genotypes after LPS treatment (Fig.4c), supporting the result of the PLX5622 experiment (Fig.3b) and thus, further implicating the significant role of microglia in this process. Therefore, we further studied the possible sites of IL-1 actions in the brain. IL-1R1 is expressed at highest levels in the brain by vascular endothelial cells[56,74,75]. In line with this, we found a significant increase of IL-1R1 expression in cerebral vessels in response to systemic inflammation (Fig.4d). To investigate whether IL-1R1 plays a functional role in this model, we first systemically administered an IL-1R1 receptor antagonist (IL-1Ra, Anakinra). Anakinra significantly reduced the number of recruited leukocytes in the cerebral cortex, as shown by CD45 immunostaining (Fig.4e). To study whether this is mediated via endothelial IL-1R1 actions, endothelial-specific IL-1R1 KO ($IL\text{-}1R1^{fl/fl\Delta Scl}$) mice were used. However, no significant change in leukocyte recruitment was found in $IL\text{-}1R1^{fl/fl\Delta Scl}$ mice (Fig.4f).

To further investigate the underlying mechanisms of IL-1R1, a detailed histological assessment was performed. First, the specificity of the antibody on IL-1R1 KO brain tissues was confirmed (Fig. S4a). As systemic inflammation resulted in increased microglial coverage of the vasculature, which was more pronounced at the venous segments (Fig.2b, e), we tested whether the morphological transformation of microglia is influenced by the presence of IL-1R1. To this end, an automated microglia morphology analysis tool was applied[76], and a 3D scatterplot was generated of analyzed microglia cells. This allowed the manual selection of microglia in contact with $IL\text{-}1R1^+$ or $IL\text{-}1R1^-$ vessels, and parenchymal microglia (with somata not contacting any vessels) (Fig. S4b, c). We found that the phenotype of vessel-associated microglia was not influenced by the presence of IL-1R1. However, parenchymal microglia displayed morphological differences compared to those in contact with blood vessels (Fig. S4c). Vessel-associated microglia displayed higher sphericity (Fig. S4d) and had fewer branching nodes (Fig. S4e) and branch ends (Fig. S4f), suggesting a more reactive morphology (Fig. S4g). To our surprise, histological investigations also revealed that IL-1R1 was not only expressed by parenchymal veins and venules, as visualized by the absence of vascular SMA labeling, confirming earlier findings[53,56,77–79], but also by meningeal and penetrating SMA-positive arteries and arterioles under systemic inflammatory conditions (Fig.4g), which still showed significantly lower levels of IL-1R1 expression compared to veins. This suggests that arterial IL-1R1 expression and changes in microglial phenotypes under systemic inflammatory conditions might be sufficient to influence leukocyte responses at the arterial side and other, related processes, such as CBF changes that could have high relevance for different CNS disease states.

Sustained systemic inflammation impairs hypercapnia-induced vasodilation through IL-1R1 and microglial IL-1α with different contribution by BAMs

Systemic inflammation can compromise CBF via different mechanisms, while accumulation of leukocytes has been implicated in vascular inflammation, injury and reduced cerebral perfusion[80–82], although their functional links and the involvement of microglial processes remained unclear. To characterize this, we measured baseline CBF and hypercapnia-induced vasodilation response (cerebrovascular reactivity) in vivo using Laser Speckle Contrast Imaging (LSCI) across the different experimental manipulations used in this study (Fig.5a). While it is considered an endothelial-driven process[83], hypercapnia serves as a well-characterized and physiologically relevant vascular challenge to probe cerebrovascular responsiveness[84,85]. We found that systemic inflammation significantly impaired both baseline CBF and hypercapnia-induced vasodilation (Fig.5b). To investigate whether systemic inflammation affects neuronal network activity that may alter cerebral blood flow, parallel EEG recordings and CBF measurements (by laser Doppler flowmetry, LDF) were carried out on a separate set of animals by an independent laboratory. EEG recordings revealed that systemic inflammation did not alter baseline neuronal activity (Fig. S5a, c, d) compared to saline-treated animals, nor did it alter neuronal activity during hypercapnic challenge. In addition, LDF also confirmed that systemic inflammation compromised cerebrovascular reactivity, as LPS-treated mice had an impaired hypercapnia-induced vasodilatory response (Fig. S5b, e), despite preserved neuronal activity. Importantly, depletion of microglia by PLX5622 reduced baseline CBF levels (Fig.5c left) and further exacerbated CBF impairments to the hypercapnic challenge (Fig.5c middle and right). In parallel, selective depletion of BAMs by clodronate (administered at day -5) did not affect baseline CBF (Fig. S5f top left), while, contrary to PLX5622, it caused improved CBF response to hypercapnia (Fig. S5f top right and

https://doi.org/10.1038/s41467-026-77787-4

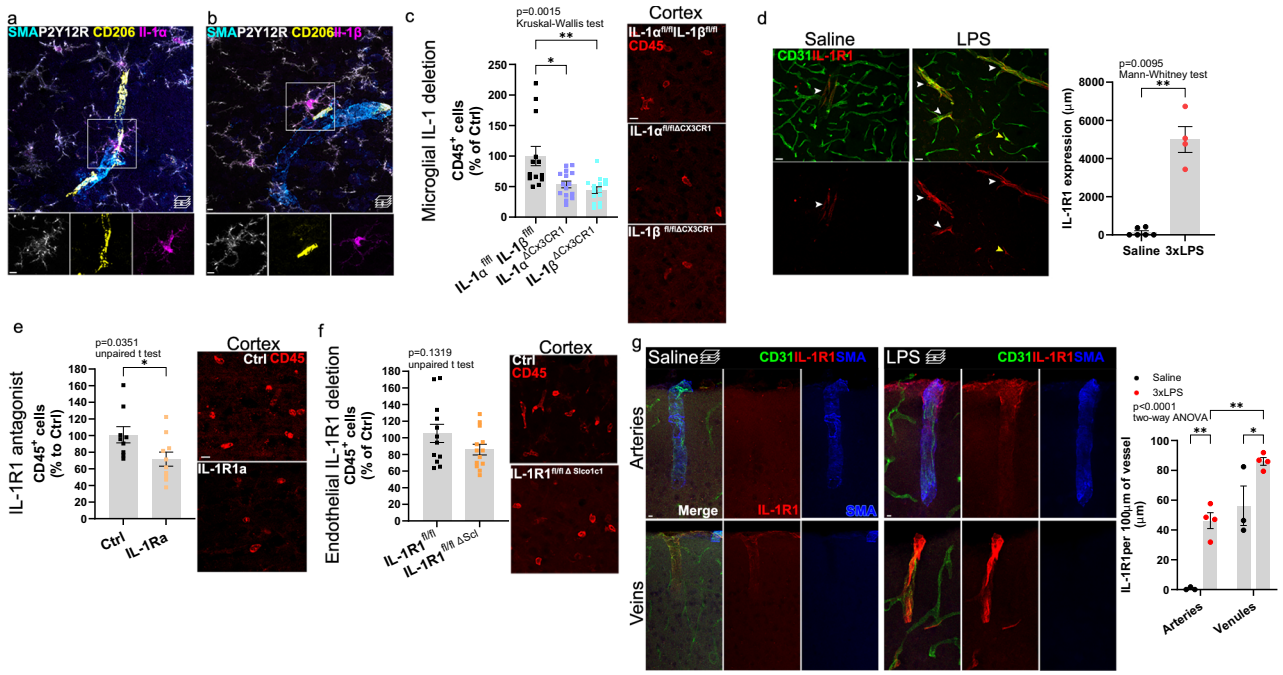

Fig. 4 | Microglial IL-1 and IL-1R1 mediate central leukocyte recruitment during sustained systemic inflammation. a,**b** CLSM MIPs showing IL-1α (**a**) or IL-1β (**b**) staining in microglia (P2Y12R$^+$ CD206$^-$) around SMA$^+$ arterioles after 3xLPS treatment. **c** Quantification of CD45$^+$ leukocytes in the cortex of conditional microglial IL-1α or IL-1β KO animals. $N = 13$ Control, $N = 14$ IL-1α KO (IL-1α$^{fl/fl\Delta CX3CR1}$) and $N = 14$ IL-1β KO (IL-1β$^{fl/fl\Delta CX3CR1}$) mice, $p = 0.0015$ Kruskal-Wallis test followed by Dunn's multiple comparisons test: $p = 0.0343$ Control vs IL-1α KO, $p = 0.0014$ Control vs IL-1β KO. **d** Total length of IL-1R1$^+$ vessels (CD31) in the cortex of saline vs LPS treated mice, $N = 6$ Saline and $N = 4$ LPS mice, $p = 0.0095$ two-tailed Mann-Whitney test. **e** Leukocyte recruitment in the cortex following systemic blockade of IL-1R1 with Anakinra (IL-1Ra), $N = 9$ Control and $N = 10$ IL-1Ra mice, $p = 0.0351$ two-tailed unpaired *t*test. **f** Leukocyte counts in the cortex of animals with endothelial-specific deletion of IL-1R1 (using IL-1R1$^{fl/fl\Delta Scl}$ mice), $N = 12$ Control and $N = 13$ IL-1R1$^{fl/fl\Delta Scl}$ mice, $p = 0.1319$ two-tailed unpaired *t*test. **g** CLSM MIPs of arterial (SMA$^+$) and venous IL-1R1 expression and corresponding quantification (intensity values expressed to 100 µm vessel length). Data are presented as mean ± SEM: **c**–**g**. Scale bars: (**a**–**c**,**e**,**f**,**g**)10 µm all; **d** 20 µm. Source data are provided as a Source Data file.

bottom). This effect was apparent both in C57BL/6 J (Control) and P2Y12R KO animals (P2Y12R is involved in microglia-mediated modulation of CBF ([7,8]) (Fig. S5f), suggesting the opposite roles of BAMs to microglia in CBF regulation under systemic inflammatory conditions. To further dissect the role of microglia and BAMs on CBF by using a genetic model, CSF1R$^{\Delta FIRE/\Delta FIRE}$ animals were used. CSF1R$^{\Delta FIRE/\Delta FIRE}$ animals reiterated the results of PLX6522-treated animals regarding a worse hypercapnic response (Fig.5d right) and elevated baseline blood flow (Fig.5d left) compared to PLX5622-treated animals, as also reported previously in the absence of systemic inflammation[86]. In line with the high number of vascularly retained leukocytes (Fig.4e, f and Fig. S4m, n) and arterial IL-1R1 expression detected (Fig.4g), we investigated the effects of IL-1 on the vasculature concerning CBF changes. We found that both IL-1Ra treatment and the absence of endothelial IL-1R1 significantly improved CBF response to hypercapnia (Fig.5e, f), suggesting the involvement of central IL-1 signaling through endothelial IL-1R1 in the regulation of cerebrovascular reactivity during systemic inflammation. In line with this, the impairment of cerebrovascular reactivity was found to be mediated by microglial IL-1, with different roles for the two IL-1 isoforms (Fig.5g). Importantly, animals lacking microglial IL-1α showed improved CBF response to hypercapnia compared to controls, while the absence of microglial IL-1β caused a significant reduction of the hypercapnic response compared to the IL-1α KO group, but did not differ from controls (Fig.5g).

Arterial leukocyte retainment correlates with impaired hypercapnic response and is modulated by microglia-derived IL-1α

Recruited leukocytes have long been recognized to contribute to vascular impairment associated with diverse inflammatory conditions[87], however, the underlying mechanisms are vaguely defined. Throughout our histological examinations, we consistently observed that recruited leukocytes remained predominantly vascularly retained (Fig. S4h–o), and adhering leukocytes were also found intraluminally in the arterial walls, not exclusively in the venous side (Fig.1g), while their functional roles remained undefined. To our surprise, a positive correlation between the number of vessel-associated leukocytes and the extent of hypercapnic response was found at the level of arteries, but not at venous side (Fig.6a), in line with increased IL-1R1 expression in penetrating arterioles in our 3x LPS model (Fig.4g). To investigate this in real time, circulating leukocytes and vasculature were visualized by i.p. injected Rhodamine 6 G[88] and SR101[89,90] and in vivo two-photon imaging was performed. Consistent with our histological data, increased number of Rhod 6 G$^+$ leukocytes were detected in 3xLPS treated animals compared to the saline group (Fig.6b,c). We found that the number of Rhod 6 G$^+$ cells significantly increased both in arteries and veins under systemic inflammatory conditions (Fig.6d–f). Arteries were clearly discriminated from veins in vivo by the presence of two-photon excited fluorescence of elastin (found only in arterial walls), detected in the green channel (Fig.6d)[91] and by confirming arterial vasomotion. Two-photon imaging revealed that the number of adhering Rhod 6 G$^+$ cells were retained for an average of 100 s in superficial penetrating arteries (Fig.6g, h and Suppl. video 1), suggesting a possible, yet unknown mechanism for leukocytes influencing arterial responses, including CBF. Importantly, we observed close proximity between microglial processes recruited to the wall of arteries and intra-vascular Rhod 6 G$^+$ leukocytes by in vivo two-photon imaging (Fig.6i, Suppl. video 2). Given that the absence of microglial IL-1α improved hypercapnic response under systemic inflammatory conditions (Fig.5g), we finally assessed the contribution of microglia-derived IL-1α in leukocyte recruitment in real time. Our data have revealed that animals depleted for microglial IL-1α (IL-1α$^{fl/fl\,\Delta CX3CR1}$ mice) have a significantly reduced number of adhering/crawling Rhod 6 G$^+$

https://doi.org/10.1038/s41467-026-77787-4

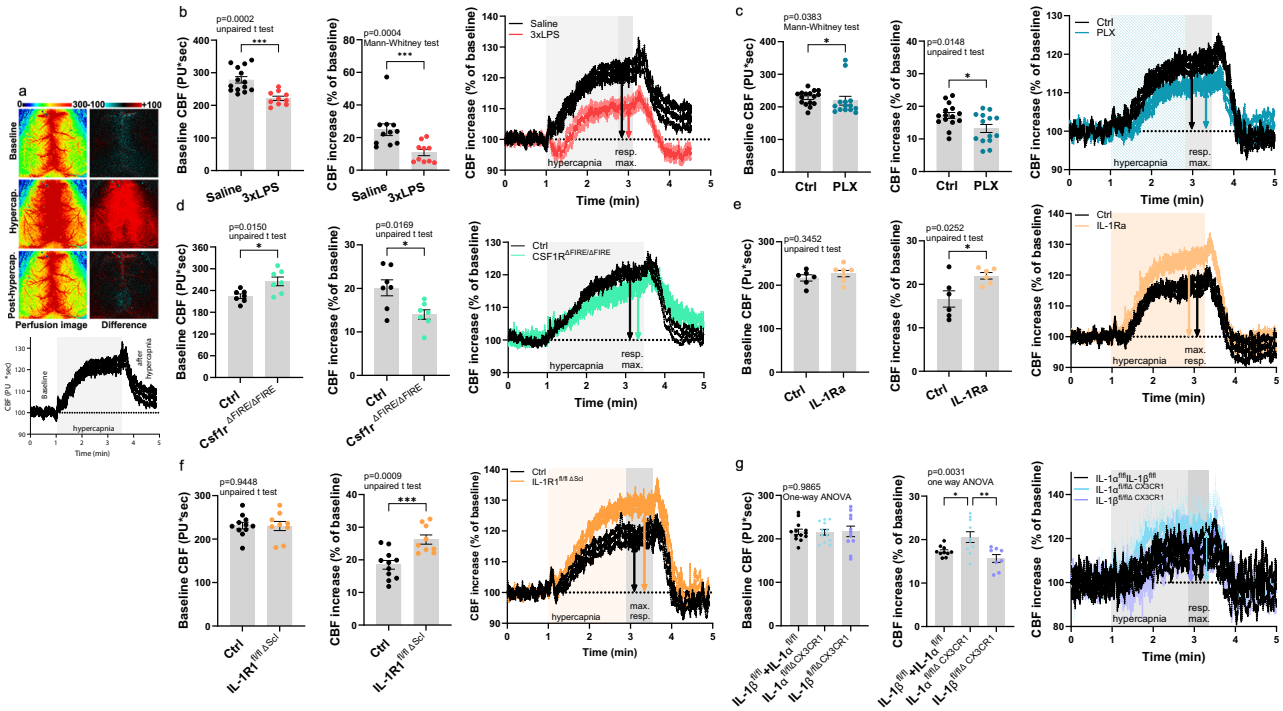

Fig. 5 | Sustained systemic inflammation impairs hypercapnia induced vasodilation mediated by microglia and microglial IL-1. a Perfusion (left) and difference (right panel) images showing the kinetics of hypercapnic response using Laser Speckle Contrast Imaging (LSCI). Experimental protocol and representative response curve of the hypercapnic challenge. **b**–**g** Baseline CBF (left) and CBF response to hypercapnia (middle) followed by a panel (right) showing representative average response curves: **b** Baseline CBF (left) upon sustained systemic inflammation induced by 3xLPS (saline vs LPS). Right panel shows representative average response curves, $N = 14$ Saline and $N = 10$ LPS mice, $p = 0.0002$ two-tailed unpaired *t*test; middle panel: $N = 11$ Saline and $N = 10$ LPS mice, two-tailed $p = 0.0004$ unpaired *t*test. **c** CBF in the absence of microglia. $N = 16$ Control and $N = 14$ PLX mice, $p = 0.0383$ two-tailed Mann Whitney test; middle panel: $N = 15$ Control and $N = 14$ PLX mice, $p = 0.0148$ two-tailed unpaired *t*test; **d** CBF in microglia depleted $CSF1R^{\Delta FIRE/\Delta FIRE}$ animals, $N = 7$ in each group, left: $p = 0.0150$ two-tailed unpaired *t*test with Welch's correction, middle: $p = 0.0169$ two-tailed unpaired *t*test with Welch's correction. **e** Pharmacological blockade of IL-1R1 using IL-1Ra (Anakinra), $N = 6$ Control and N = 7 IL-1Ra mice on both panels, $p = 0.0252$ two-tailed unpaired t-test. f CBF upon endothelial IL-1R1 deletion $N = 11$ Control and $N = 9$ IL-1R1 KO ($IL\text{-}1R1^{fl/fl\Delta Scl}$) mice on both graphs. $p = 0.0009$ two-tailed unpaired *t*test; **g** microglial IL-1α or IL-1β deletion, $N = 13$ Control, $N = 12$ IL-1α KO ($IL\text{-}1\alpha^{fl/fl\Delta Cx3CR1}$) and $N = 11$ IL-1β KO ($IL\text{-}1\beta^{fl/fl\Delta Cx3CR1}$) mice, $p = 0.9865$ one way ANOVA followed by Tukey's multiple comparison test. Middle panel: $N = 10$ Control, $N = 10$ IL-1α KO and $N = 8$ IL-1β KO mice, $p = 0.0031$ one way ANOVA followed by Sidak's multiple comparisons test: $p = 0.043$ Control vs IL-1α KO, $p = 0.0032$ IL-1α KO vs IL-1β KO. All data in the figure are presented as mean ± SEM. All animals were measured by LSCI and were subjected to the same 3xLPS protocol before hypercapnic challenge. Source data are provided as a Source Data file.

cells in the arteries compared to controls, with increased adherence time (Fig.6j, l). In line with this, the absence of microglial IL-1α did not affect the number of adhering leukocytes, but reduced their adherence times in veins (Fig.6k, l). These results suggest that microglial IL-1α could have different effects on arterial and venous leukocyte responses, linking leukocyte recruitment with CBF changes under systemic inflammatory conditions.

Discussion

Here, we studied the contribution of microglia and BAMs to leukocyte recruitment and associated CBF responses under sustained systemic inflammation. Our data suggest that microglia and BAMs not only play opposing roles in these processes, but intra-arterial leukocytes may also influence CBF responses in a microglia-dependent manner. We identify microglial IL-1α linking leukocyte – vascular cross-talk with impaired hypercapnia-induced vasodilation on the arterial side, while both IL-1 isoforms promote leukocyte recruitment in different vascular beds across the brain.

These observations may be relevant for diverse inflammatory brain pathologies. Leukocyte recruitment to the CNS is a characteristic feature of multiple sclerosis (MS) and its established animal model, EAE[92,93], stroke[94], traumatic brain injury[95], meningeal infections[96–98] and tumors[99], among other conditions with indirect CNS effects, such as chronic liver disease[100]. Accumulation of neutrophils, monocytes or T-cells occurs before clinical manifestation of EAE and in murine models of vascular dementia, while blockade of leukocyte recruitment or IL-1 signaling attenuates BBB breakdown, vascular inflammation, and neuronal death in experimental models of systemic inflammation and stroke[32,53,55,101–103]. However, the mechanisms whereby central myeloid cell populations regulate systemic inflammation-related leukocyte recruitment and CBF changes are largely unclear. The limited availability of tools to selectively modulate microglia and BAMs underlies conflicting reports regarding their roles in leukocyte-vessel interactions, BBB integrity, or changes in CBF[5]. In addition, central myeloid cell responses may be markedly altered across different inflammatory or disease states. For example, while PVMs support the integrity of the BBB under physiological conditions[104,105], they contribute to BBB injury[105,106] and Aβ-induced neurovascular dysfunction in AD[107] or hypertension[108]. Accordingly, depletion of PVMs attenuated BBB leakage in a hypertension model[109] and ameliorated neurovascular coupling response in chronically hypertensive mice[38] and in Aβ-induced cerebrovascular dysfunction[107], with attenuated hypertension-induced vascular remodeling and improved vasodilation in hypertensive rats[110]. In line with this, BAMs promote recruitment of granulocytes in the acute phase of stroke[111] and in bacterial meningitis[112], while recruiting monocytes and T-cells in HIV-associated encephalitis and EAE[96] or in Theiler's murine encephalomyelitis virus (TMEV) infection[113]. Our present findings align with recent data showing that BAM depletion exacerbates leukocyte infiltration following ischemic stroke in aged mice[65]. However, methodological

https://doi.org/10.1038/s41467-026-77787-4

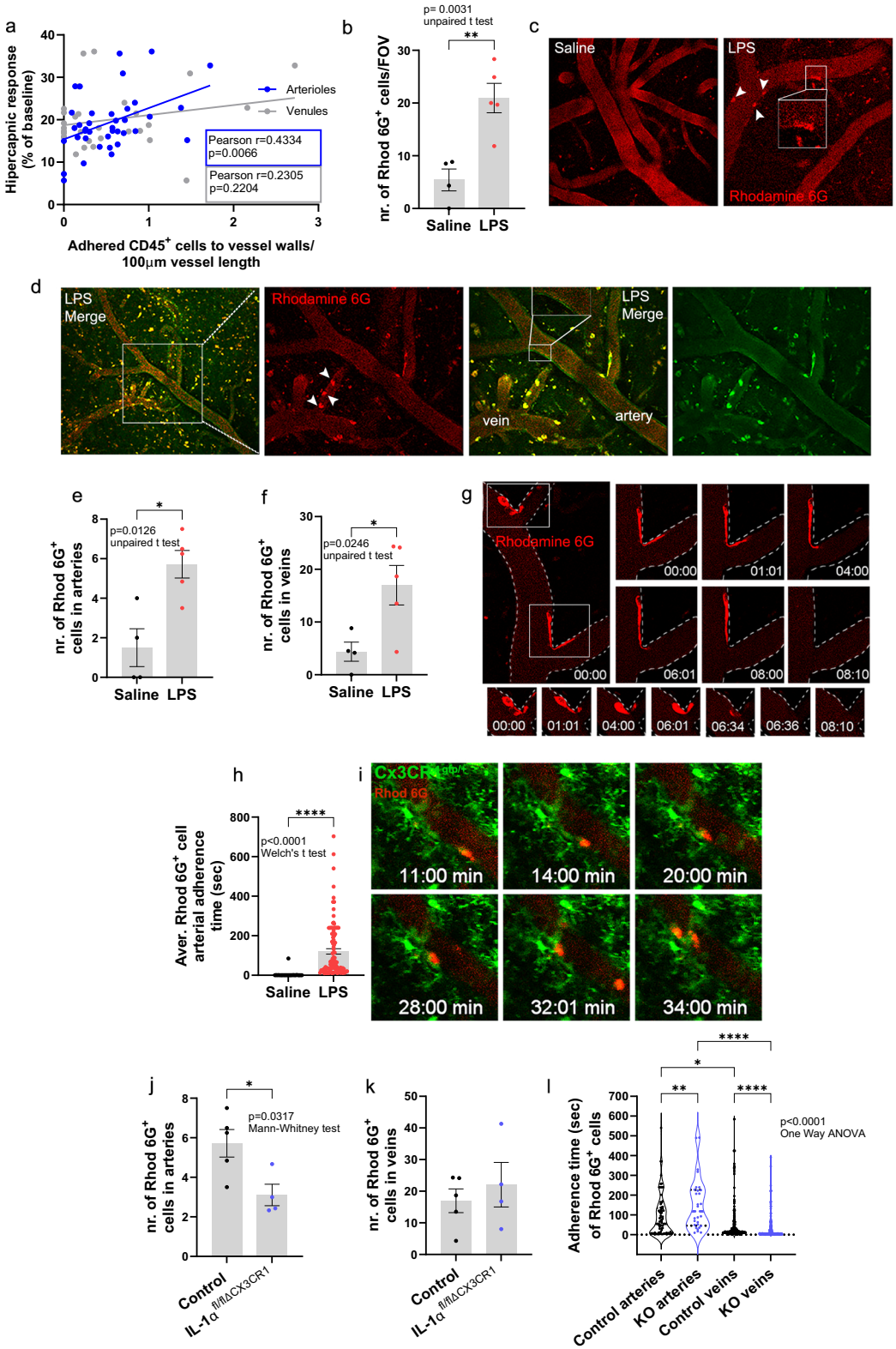

considerations concerning selectivity, efficacy, and potential off-target effects of clodronate, PLX5622, and other tools apply when drawing conclusions from cell depletion studies. To overcome this issue, CSF1R$^{\Delta FIRE/\Delta FIRE}$ mice were used to dissect the role of BAMs and microglia in a genetic model without acute cell depletion. CSF1R$^{\Delta FIRE/\Delta FIRE}$ mice lack CSF1R expression due to the elimination of FIRE (fms-intronic regulatory element) from the Csf1r locus and do not possess microglia throughout their life, while BAM populations are well preserved[70]. Importantly, we found that microglia play opposing roles to BAMs under systemic inflammatory conditions. The absence of parenchymal microglia after both PLX5622 treatment and in CSF1R$^{\Delta FIRE/\Delta FIRE}$ mice reduced leukocyte recruitment, while clodronate treatment increased it. We propose that, concerning parenchymal tissues and vasculature, the overall impact of microglia depletion is dominant over

Fig. 6 | Arterial leukocyte recruitment correlates with impaired hypercapnic response and is modulated by microglial derived IL-1α. a Pearson correlation between the number of arterial or venous CD45$^+$ cells and the hypercapnic response in $N = 79$ Control animals, pooled from all experiments in the 3xLPS model. Arterioles: r = 0.4334, $p = 0.0066$. Venules: r = 0.02305, $p = 0.2204$. **b** Number of Rhodamine 6 G$^+$ cells/area imaged by in vivo two-photon microscopy, $N = 4$ Saline and $N = 5$ LPS mice, $p = 0.0031$ two-tailed unpaired *t*test. **c** Two-photon images of Saline vs LPS mice showing Rhodamine 6 G$^+$ cells on an SR101 labeled vascular background. Arrowheads point at recruited cells. d Rhodamine 6 G$^+$ cells in arteries and veins after 3xLPS, distinguished by the presence of in vivo two-photon excited fluorescence of the arterial elastin layer on the green channel (also shown by the insert). **e**,**f** Number of Rhodamine 6 G$^+$ cells in arteries and veins in $N = 4$ Saline and $N = 5$ LPS mice, $p = 0.0126$ two-tailed unpaired *t*test for arteries, p = 0.0246 two-tailed unpaired *t*test for veins. **g** In vivo two-photon recording of arterial wall-adherent Rhodamine 6 G$^+$ cells on an SR101-labeled vascular background. **h** Average arterial adherence time of individual Rhodamine 6 G$^+$ cells that stayed more than 10 s at the arterial wall, $N = 24$ saline and $N = 103$ LPS cells derived from $N = 4$ saline and **N** = 5 LPS animals, $p = 0.0001$ two-tailed unpaired *t*test with Welch's correction. **i** Examples for in vivo interactions between microglial processes (green, in CX3CR1$^{gfp/+}$ mice) and Rhodamine 6 G$^+$ (red) cells in LPS treated mice on an SR101 labeled vascular background. **j**,**k** Number of intra-vascular Rhodamine 6 G$^+$ cells in control vs microglial IL-1α KO arteries and veins (in IL-1α$^{fl/fl\,\Delta\,CX3CR1}$ mice), $N = 5$ control and $N = 4$ IL-1α$^{fl/fl\,\Delta\,CX3CR1}$ mice, $p = 0.0317$ two-tailed Mann-Whitney test for arteries. **l** Average intravascular adherence time in control vs microglial IL-1α KO arteries and veins, $N = 4$ mice per group, $p < 0.0001$, One-Way ANOVA with Sidak's multiple comparison: $p = 0.0050$ for Control vs microglial IL-1α KO arteries, $p < 0.0001$ for Control vs microglial IL-1α KO veins, $p = 0.0252$ for Control arteries vs Control veins, $p < 0.0001$ for microglial IL-1α KO arteries and microglial IL-1α KO veins; Data are presented as mean/animal±SEM: **a**,**b**,**e**,**f**,**j**,**k**,**l**. Source data are provided as a Source Data file.

PVM effects in this experimental model, as suggested by reduced leukocyte numbers even in the absence of both microglia and PVMs after PLX5622 treatment, with similar effects seen in CSF1R$^{\Delta FIRE/\Delta FIRE}$ mice possessing an intact PVM niche. In the meninges, PLX5622 and clodronate also showed opposing effects, strengthening the different roles of microglia and BAMs. In the CSF1R$^{\Delta FIRE/\Delta FIRE}$ study, preserved meningeal macrophages, the distance of the microglial compartment to the meninges in control mice, and possible, yet unknown, compensatory effects in BAMs of CSF1R$^{\Delta FIRE/\Delta FIRE}$ mice may explain the lack of differences seen in recruited leukocyte numbers in the meninges, which should be investigated in future studies.

We also found that microglia and BAMs shape CBF responses differently in this systemic inflammation model. Under physiological conditions, microglia contribute to functional hyperemia and hypercapnia-induced vasodilaion[7,8], and support adaptation to cortical hypoperfusion via the purinergic receptor P2Y12R that is microglia-specific in the brain[8]. However, the operation of these microglial modulatory actions under systemic inflammatory conditions has remained unclear to date. Importantly, we found that microglia but not BAMs, remained essential for supporting hypercapnia-induced vasodilation even in the inflamed brain, as evidenced by both PLX5622 treatment and CSF1R$^{\Delta FIRE/\Delta FIRE}$ mice, while BAM depletion by clodronate showed an opposite effect. In line with this, downregulation of microglial P2Y12R in our 3xLPS model is likely to impair the CBF regulatory functions of microglia, which could have far-reaching consequences in the aged brain or in diverse disease states, where downregulation of P2Y12R reportedly occurs[17,114–116]. Although we did not find increased BBB permeability in this model, our findings confirm earlier observations showing that LPS-induced inflammation increases microglia-blood vessel association and disintegration of astrocytic endfeet that could involve phagocytic activity of microglia[18]. We also confirm observations regarding systemic inflammation-related leukocyte recruitment[117–120], altered microglial morphology[121,122] and changes in microglia-vascular interactions[77,123].

Although vascular-associated microglia presented distinct morphological features compared with parenchymal cells, we found no difference between microglia associated with IL-1R1$^+$ or IL-1R1$^-$ vessels considering all vascular beds. Surprisingly, we revealed that microglial IL-1α is a major contributor to leukocyte recruitment under systemic inflammatory conditions related to CBF changes at the level of arteries, as also suggested by LPS-induced increases in arterial IL-1R1 levels. These findings may explain the complex roles of endothelial IL-1R1 in this experimental model, concerning the reduced number of recruited CD45$^+$ cells and concomitant CBF improvement after IL-1Ra treatment, whereas improved CBF responses and the lack of effect by endothelial IL-1R1 deletion on leukocyte numbers. Supporting this, lack of an effect of IL-1R1 deletion on leukocyte recruitment to the brain has also been shown by others[52], while conditional deletion of endothelial IL-1R1 was found to improve perfusion deficits after cerebral ischemia[53]. However, effects of ICV-injected IL-1β were found to be mediated by endothelial IL-1R1[49] with similar findings presented concerning leukocyte recruitment in EAE[62]. These results suggest complex, possibly multicellular roles for IL-1R1 signaling in the recruitment of leukocytes to the CNS and CBF changes that could involve astrocytes or other parenchymal cells and different contributions by endothelial IL-1R1 in different vascular beds.

To investigate microglia-vascular-leukocyte interactions in real time, in vivo two-photon imaging was performed. Consistent with our histological data, systemic inflammation increased the number of Rhod 6 G$^+$ leukocytes both in arteries and veins, alongside their retention near vessel-associated microglial processes. We found both microglial IL-1α and IL-1β to be important drivers of leukocyte recruitment, while playing different roles in cerebrovascular reactivity. In line with improved CBF responses, in vivo two-photon imaging revealed a 50% reduction of Rhod 6 G$^+$ cells in arteries of microglial IL-1α KO animals, while adherence times of intra-arterial leukocytes were significantly prolonged compared to the veins. These observations raise a possible role for recruited leukocytes in CBF impairments in this model, which will need to be functionally studied in other brain pathologies with underlying central or systemic inflammation. In summary, microglia emerge as key modulators of leukocyte recruitment to the brain and systemic inflammation-associated hypoperfusion, with distinct roles from BAMs. Understanding the modulatory actions of different brain myeloid cells may pave the way for the identification of novel therapeutic targets in CNS disorders.

Methods

Animals

All animals were maintained at 21 °C ± 1 °C, 55 ± 10% humidity, in a 12 h light-dark cycle with food and water *ad libitum*. All experiments were in accordance with the guidelines set by the European Communities Council Directive (86/609 EEC) and the Hungarian Act of Animal Care and Experimentation (1998; XXVIII, Sect. 243/1998), approved by the Animal Care and Experimentation Committee of the HUN-REN Institute of Experimental Medicine and the Government Office of Pest County Department of Food Chain Safety, Veterinary Office, Plant Protection and Soil Conservation Budapest, Hungary, under the numbers PE/EA/ 1021-7/2019 and PE/EA/673-7/2019. Experiments were performed according to EU Directive 2010/63/EU on the protection of animals used for scientific purposes and are reported in compliance with the ARRIVE guidelines.

All Experiments were carried out on 3–6 months-old male mice, all on C57BL/6 J (Jax strain#000664) background. Full P2Y12R KO (Deltagen Cat# EM:02301[124],) and IL-1R1 KO mouse[125] lines were used. Csf1r$^{\Delta FIRE/\Delta FIRE}$ mice (Jax strain #032783[70],) were obtained in collaboration with Clare Pridans, University of Edinburgh. The generation of

systemic endothelial IL-1R1 KO (IL-1R1$^{fl/fl\ \Delta Scl}$) animals was achieved by crossing the endothelial-SCL^{CreERT} (Jax strain#037467[126],) line with the IL-1R1$^{fl/fl}$[125] mouse line. Microglial IL-1α or IL-1β depletion (microglial IL-1α$^{fl/fl\ \Delta\ CX3CR1}$ (referred as IL-1α KO) or IL-1β$^{fl/fl\ \Delta CX3CR1}$ (referred as IL-1β KO)) was achieved by crossing the IL-1α$^{fl/fl}$[127] or the IL-1β$^{fl/fl}$[128] mice with the Cre-expressing CX3CR1^{CreERT2} mouse line (Jax strain# 020940). Cell-specific deletions were achieved by two i.p. injections of tamoxifen (2 mg, dissolved in corn oil, Sigma), 48 h apart at 4–6 weeks of age. Control mice (corresponding fl/fl lines) also received tamoxifen. All experiments were carried out at least 3 weeks after tamoxifen treatment.

Induction of sustained systemic inflammation

Animals were treated daily with a single lipopolysaccharide (LPS, E. coli serotype O26:B6, Sigma #L8274) injection for three consecutive days with 2-2-1 mg/kg dose intraperitoneally (i.p.). Saline-treated animals received 100 μl i.p. injections of physiological saline. In every set of experiments, the control and all corresponding treatment groups received the same LPS treatment, unless otherwise stated. Animals were sacrificed 24 hours after the third LPS dose (otherwise stated), while blood, brain and peripheral organs were collected and stored for future experiments. Brain tissues were always processed for anatomical analyses. The health status of the animals was strictly monitored throughout the experiment, and hydration of animals was ensured by daily subcutaneous physiological saline injections. In case of severe sickness behavior symptoms (fever, piloerection, loss of appetite, immobility) the animals were terminated.

Tissue processing

Terminally anaesthetized mice (with ketamine-xylazine) were transcardially perfused and fixed with 4% phosphate-buffered paraformaldehyde (PFA, pH 7.4) using a slow flow rate (15 rpm). Then, PFA was washed out with 0.1 M phosphate buffer (PB, pH 7.4) for 2 minutes. Brains were collected and stored in 0.01% sodium azide containing 0.1 M PB until sectioning. Coronal sections with 40 μm (for regular immunostainings) or 100 μm (for automated microglia analysis) thickness were obtained alternately from the same brain using a vibratome (VT1200S, Leica, Germany).

Immunofluorescence

Free-floating sections were washed in Tris-buffered saline (0,05 M TBS) before blocking with 5-10% normal donkey serum (Jackson ImmunoResearch), then incubated with primary antibodies O/N at 4 °C (for a detailed list of antibodies used, see Supplementary Table 1). Sections were washed and incubated with the corresponding secondary antibodies for 2 h at RT (see Supplementary Table 2 for full antibody list). Finally, they were mounted on glass slides (using Fluoromount-G, #0100-01, SouthernBiotech).

Pictures were acquired using a Nikon Eclipse Ti-E inverted CLSM microscope (Nikon Instruments) equipped with a Plan Apochromat VC 20x objective (NA 0.75), 60x water immersion objective (NA 1.2), and an A1R laser confocal system, as otherwise stated. The following lasers were used: 405, 488, 561, and 647 nm (CVI Melles Griot). Scanning was done in line serial mode. Images were obtained with NIS-Elements AR5.42.02 software.

Image analysis

Leukocyte recruitment: Whole slides were scanned (using a Panoramic MIDI II slide scanner, 3DHISTECH, Hungary) and selected fields of view (FOVs) with a fixed area of 0.446mm^2 (for cells/area quantifications) or 0.309 mm^2 (for vessel length measurements) were analyzed using the SlideViewer (3DHISTECH) software. For quantifications, a minimum of 4 different coronal sections with 4–6 individual FOVs were selected per animal. The number of cells per FOV (microglia, leukocytes, monocytes, neutrophils, BAMs or pericytes) was manually counted in line with the measurement of vessel lengths using the annotation tool of 3DHISTECH. For all quantifications, FOVs were consistently selected within the same coronal sections from the cortical region spanning from the anterior cingulate area to the somatosensory cortex, unless otherwise specified (e.g., when the striatum was analyzed). Cell counts were averaged per animal and displayed on graphs as mean ± SEM, otherwise indicated. Due to the highly variable effect of LPS, every set of experiment included appropriate controls, and data were expressed as a percentage of the corresponding control group. For quantification of leukocytes in the meninges, the length of meningeal vasculature was delineated using a vascular marker, and leukocyte numbers were counted along this length. Cell counts were expressed as per mm of meningeal length, averaged per animal, and expressed as a percentage of the corresponding control group.

For microglial process coverage of cerebral blood vessels, confocal pictures of 4 sections/animal (1 ROI/section) with vascular labeling (laminin α2 and SMA) and microglia (Iba1) were analyzed with a semi-automated method in FIJI (at least 3 ROIs/ /animal). Briefly, images were opened in FIJI, and vessels were manually masked as individual ROIs based on laminin α2 or SMA labeling. The selected ROIs were overlaid onto a binary image of the microglia channel, and the "Multi Measure" function was used to quantify the % area occupied by microglial pixels within each ROI. Identification of the arterial-venous vascular segments was based on vascular diameter and the presence of SMA. Based on these criteria, arterioles (SMA signal), capillaries (low laminin α2 signal, diameter <10 μm), postcapillary venules (high laminin α2 signal, 10 μm < diameter < 20 μm) or venules (high laminin α2 signal, diameter >20 μm) were discriminated and the percentage area covered by microglia was determined.

To evaluate ICAM-1 signal intensity on the brain vasculature, integrated density was measured on confocal images acquired using a Nikon Ni C2 (Nikon Instruments) microscope equipped with a Plan Apochromat VC 20x objective (NA 0.75). Pictures were taken from the somatosensory cortical region of sections stained for ICAM-1 and laminin α2 (see Supplementary Table 1). The ICAM-1 channel was manually thresholded in FIJI and integrated density was measured in 4 sections/animal (1 ROI/section).

Lipocalin2 and ZO-1 Integrated Density quantification

In FIJI, using CSLM images (single layer for Lcn2) and MIPs (for ZO-1) ROIs were defined on the CD31 channel to outline vessels. For each animal, four vascular segments—each obtained from a different coronal slice—were analyzed. Within each ROI the IntDen for Lcn2 or ZO-1 (see Supplementary Table 1) was measured and averaged per animal.

To investigate whether IL-1R1 expression increases in cerebral vessels upon LPS treatment, IL-1R1 expression was quantified. Whole-slide images acquired with a slide scanner (Panoramic MIDI II slide scanner, 3DHISTECH, Hungary) were analyzed. For each animal, three to four identical coronal sections were selected and stained with CD31 and IL-1R1 (see Supplementary Table 1). A defined area (approximately 8 mm^2) was preselected in the cortex and manual quantification was performed using the annotation tool of the slide scanner software. Within each ROI, CD31+ vessels exhibiting IL-1R1 immunoreactivity were traced, and the total length of IL-1R1-positive vessel segments was recorded and summarized per animal.

To evaluate IL-1R1 expression in penetrating vessels, whole-slide images acquired with a slide scanner (Panoramic MIDI II slide scanner, 3DHISTECH, Hungary) were analyzed. For each animal, 2-3 brain sections were stained for CD31, SMA, and IL-1R1 (see Supplementary Table 1). Penetrating vessels were identified based on CD31 and SMA channels, which allowed differentiation between venules and arterioles. The length of each CD31$^+$ and IL-1R1$^+$ vessel was measured using the slide scanner software. Subsequently, the length of IL-1R1-positive segments were expressed relative to the total CD31+ vessel length, averaged per animal and calculated to 100 μm vessel length.

Magnetic resonance imaging (MRI)

MRI measurements, combined with the use of microsized particles of iron oxide (MPIOs) conjugated with anti-VCAM-1 or IgG antibodies, were performed as described previously[48,129] to address endothelial activation and BBB leakage. In brief, rat anti-mouse antibodies for VCAM-1 or control rat IgG were covalently conjugated to MPIOs (1.08 µm diameter) in borate buffer (pH 9.5) at 37 °C for 48 h. The coating contained 10 µg VCAM-1 or 10 µg IgG antibody per 1 mg reactive MPIO. After, beads were washed and incubated with PBS containing 0.5% BSA for 24 h at room temperature to block remaining active groups. MPIO solution was stored under continuous rolling at 4 °C until usage. Animals were injected intravenously through the tail vein with 200 µl (0.25 mg of beads) of coated MPIO solution immediately before imaging. Imaging was performed on a Pharmascan 7 T/12 cm system using surface coils (Bruker, Germany). MRI was performed with 3D T2*-weighted imaging (spatial resolution of 70 × 70 x 70 mm interpolated to an isotropic resolution of 70 mm), TE/TR 13.2 ms/200 ms and a flip angle of 21° was performed to visualize MPIOs. All T2*-weighted images presented are minimum intensity projections of six consecutive slices. Analysis of the MPIO signal voids on 3D T2*-weighted images was made by ITK Snap; an open-source and multi-platform 3D medical image analysis software, optimized for user-guided segmentation[130]. The void of MPIO-signal was manually quantified from the 3D T2*-weighted images, and the results are presented as nr of voxels/brain. For Gadolinium detection of BBB leakage, 3D T1 FLASH sequences (spatial resolution 70 mm*70 mm; TE/TR 4.46/15; 3 averages; 4 min 2 s) were used, 15 min after the i.p. injection of Gadolinium chelate (DOTAREM) diluted in saline (0,5 mmol/ml). As no extravasation was observed, no quantification was performed.

Flow cytometry

Recruited leukocyte populations were characterized using flow cytometry. Animals were transcardially perfused with saline, and brains were harvested. In Saline vs LPS experiment (Fig.1) brain cortex was enzymatically digested at 37 °C for 10 min with constant shaking in a mixture of collagenase D (0.5 mg/mL, #11088866001, Roche) and DNase I (10 µg/mL, #DN25, Sigma-Aldrich) prepared in DMEM (#6546, Sigma-Aldrich) supplemented with 10% FBS. The digested cell suspension was filtered through a 40 µm cell strainer (Corning) and resuspended in a 40% Percoll solution before being overlaid onto a 70% Percoll layer (#17-0891-01, GE Healthcare). Percoll gradient was centrifuged at 2,100 rpm for 30 minutes, and cells were collected from the 40%/70% interphase.

In BAM depletion experiment, whole brains were mechanically homogenized using a Potter tissue grinder in (HBSS) containing 15 mM HEPES and 0.54% glucose. Homogenates were subjected to 37% Percoll gradient centrifugation at 800 × g for 30 min at 4 °C (without brake), and the resulting cell pellet was washed in 2% FBS containing PBS. Isolated cells were incubated with anti-mouse CD16/32 (Fc block; BD Biosciences, clone 2.4G2; #553142) at 4 °C to prevent non-specific Fc receptor binding (15 min). Cells were then stained at 4 °C for 30 minutes with fluorochrome-conjugated antibodies, including: CD11b (eBioscience, #11-0112-81, 1:200), Ly6C (eBioscience, #25-5932-80, 1:500), Ly6G (BioLegend, #127613, 1:500), P2Y12 (BioLegend, #848003, 1:200), CX3CR1 (BioLegend, #149037, 1:200), CD45 (BioLegend, #103131, 1:200); and CD45 (BD Biosciences, 30-F11), Ly6G (BD Biosciences, 1A8), CD4 (BD Biosciences, RM4-5), CD8a (BD Biosciences, 53-6.7), CD206 (BioLegend, C068C2), P2Y12R (BioLegend, 848004), and anti-CD90.2 (Thy1.2, clone 30-H12, BioLegend). Isotype controls were used to define gating parameters. Samples were washed and analyzed on a BD FACSVerse™ flow cytometer using BD FACSuite™ v1.0.6. software. Data were processed with FlowJo v7.6.5 (TreeStar). Live/dead cell discrimination was performed using Zombie Violet, and absolute counts were determinded using 15µm polystyrene counting beads (#18328–5, Polysciences) and expressed per mg tissue (Fig.1j) or as percentage of live, singlet events (Fig.S3b).

STED superresolution imaging and quantitative analysis

Immunofluorescent labeling was performed as described above in 2 animals from each treatment group. The primary antibodies used were: P2Y12R, Iba1, Aqp4. We also used Biotinylated Tomato Lectin (Vestorlabs, B-1175, 1:500 dilution). Samples were mounted with SlowFade™ Diamond Antifade Mountant (Thermo Fisher Scientific, S36967). Immunofluorescence was analyzed using an Abberior Instruments Facility Line STED Microscope system built on an Olympus IX83 fully motorized inverted microscope base (Olympus), equipped with a ZDC-830 TrueFocus Z-drift compensator system, an IX3-SSU ultrasonic stage, a QUADScan Beam Scanner scanning head, APD detectors, and an UPLXAPO60XO 60X oil immersion objective (NA 1.42). We used the 405, 488, 561 and 640 nm solid state lasers for imaging, and a 775 nm solid state laser for STED depletion. Image acquisition was performed using the Imspector data acquisition software (version: 16.3.14278-w2129-win64). Measurements were performed with the FIJI software package. Single high-resolution CLSM/STED image planes were used, and microglial processes were identified based on Iba1 staining on the CLSM channel. After thresholding the CLSM channel, processes that contacted vascular elements were delineated, and their outlines were used as respective ROIs. The integrated fluorescent density of P2Y12R-labeling (P2Y12R intensity) was measured within these ROIs using the P2Y12R-STED channel. Next, the clusters within these ROIs were identified automatically by thresholding, and cluster sizes (P2Y12R cluster size) along with cluster densities (cluster/ROI area) were measured. Finally, we used the outlines of individual clusters on the original untresholded STED images to extract fluorescent intensity values (P2Y12R intensity within clusters) for each cluster corresponding to their P2Y12R-content. P2Y12R intensity, P2Y12R cluster size, cluster density, and P2Y12R intensity within clusters are distinct parameters: “P2Y12R intensity” reflects to full receptor expression (both intra- end extra-cluster), “cluster size” represents the spatial properties of distinct receptor assemblies, “cluster density” shows the number of individual clusters on a given surface area, while “P2Y12R intensity within clusters” represents the amount of receptor proteins within individual clusters. To assess the continuity/integrity of Aqp4-positive endfeet around vascular elements, we measured the Aqp4 fluorescent intensity along a 300 nm wide ribbon-shaped ROI (% of vascular surface with low Aqp4 intensity) that incorporated the peri-vascular Aqp4 signal. Fluorescent intensity (Aqp4 Intensity over cutoff) was plotted as a function of distance along the perimeter of the vasculature (i.e., along the ribbon-shaped ROI). Abrupt Intensity Drop (AID) was determined as at least 40% drop of maximal intensity within a 0.8 µm distance along the vascular profile. The higher the density of AIDs is around a vessel, the lower the continuity/integrity of the endfeet coverage.

Pre-embedding immunogold labeling

After extensive washes in 0.1 M PB and 0.05 M TBS (pH 7.4), free-floating vibratome sections were blocked in 1% Human Serum Albumin (HSA). Then, they were incubated with rabbit anti-Iba1 antibody (see Supplementary Table 1) in TBS for 3 days. After several washes, sections were incubated in blocking solution (Gel-BS) containing 0.2% cold water fish skin gelatine and 0.5% HSA for 1 h. Next, sections were incubated with 1.4 nm gold-conjugated goat anti-rabbit Fab fragment (1:100, #2004 Nanoprobes) diluted in Gel-BS overnight. After extensive washing, sections were treated with 2 glutaraldehyde for 15 min to fix the gold particles into the tissue. To develop the immunogold reaction, sections were incubated in silver enhancement solution (SE-EM; Aurion) for 60 min at RT. The sections were then treated with 1% OsO4 in PB at RT, washed, treated with 1% uranyl acetate in DW for

20 min, dehydrated in an ascending alcohol series and in acetonitrile, and were embedded in Durcupan (ACM; Fluka). For electron microscopic analysis, tissue samples from the somatosensory cortex (S1) were glued onto Durcupan blocks. 100nm-thick sections were cut using an ultramicrotome (Leica EM UC7) and picked up on Formvar-coated single-slot grids.

Electron tomography, analysis

Before electron tomography, serial sections on single-slot copper grids were photographed with a Hitachi H-7100 electron microscope and a Veleta CCD camera. Serial sections were examined at lower magnification, and Iba1-positive microglial processes contacting the vasculature were selected. After this, grids were put on drops of 10 % HSA in TBS for 10 minutes, dipped in distilled water (DW), put on drops of 10 nm gold conjugated Protein-A (Cytodiagnostics #AC-10-05) in DW (1:3), and washed in DW. Electron tomography was performed using a Thermo-Fisher (FEI/Tecnai) T12 BioTwin electron microscope equipped with a computer-controlled precision stage (CompuStage, FEI), and a Xarosa 20MP bottom-mounted CCD camera (Emsis GmbH, Germany). Acquisition was controlled via the SerialEM[131]. Regions of interest were pre-illuminated for 4-6 minutes to prevent further shrinkage. Tilt series were collected at 2-degree increment steps between -60 and +60 degrees at 120 kV acceleration voltage and 23000x magnification with -1.6 – -2 μm objective lens defocus. Reconstruction was performed using the IMOD software package[132]. Isotropic voxel size was 0.41 nm in the reconstructed volumes.

Automated microglial morphology analysis

100 μm thick free-floating sections were stained for cell nuclei (DAPI, Sigma 10236276001), microglia (Iba1), IL-1R1 and vasculature (CD31, see Supplementary Table 1). Confocal stacks were acquired with 0.2 μm/pixel resolution and 0.4 μm Z-step using Nikon A1R confocal microscope with 60x water immersion objective (NA 1.2; Nikon Instruments). Stacks were acquired from the cortical somatomotor region and were analyzed using the open-source MATLAB-based Microglia Morphology Quantification Tool (MMQT, available at https://github.com/isdneuroimaging/mmqt). This automated analysis platform provides an unbiased, 3D analysis of microglia morphology, using only microglial and nucleic labeling to identify individual cells[76]. Afterwards, individual cells were manually grouped into the following categories: microglia around IL-1R1^{+} or IL-1R1^{-} vessels and parenchymal cells. Briefly, using the coordinates of the cells identified in the automated analysis, a 3D scatter was obtained in MATLAB and correlated to the stack containing all the channels to identify cells sitting on the vasculature.

Depletion of microglia or BAMs

To deplete microglia, C57BL/6 J animals were fed a PLX5622 (containing 1200 mg/kg CSF1R inhibitor) diet for 3 weeks. Depletion efficacy was validated by Iba1 immunostaining. Mice with less than 90% depletion efficacy were excluded from any further analysis. LPS treatment started on 17th day of PLX diet, the experiment ended at 21st day of microglia depletion. In order to deplete BAMs, central clodronate administration was used. Mice under 1.5% isoflurane anesthesia were securely placed on a stereotaxic frame. Then, the cisterna cerebellomedullaris magna was surgically exposed and using a glass capillary, 100 μg (in 5 μl volume) clodronate (#F70101C-AH-FOR High Potency Clophosome-A, Stratech) was slowly injected, while control animals received an i.c.m. injection of vehicle (PBS) or control liposomes. A single clodronate treatment is sufficient for depleting BAMs for 10 days. Treatments with LPS started 24 h (referred to as clodronate day 0) or 5 days (referred to as clodronate day -5) after i.c.m. clodronate administration.

Laser speckle imaging (LSCI)

Hypercapnic challenge was performed uniformly on all animals used for histological investigations and treated with our LPS model before perfusion for anatomical studies. Mice were placed on a stereotaxic frame under a sedative dose of ketamine-medetomidine (i.p. 30 mg/kg ketamine- 0.1 mg/kg medetomidine) to measure CBF using a PeriCam PSI High Resolution LSCI system (Perimed AB, Järfälla-Stockholm, Sweden) at 21 frames/s frequency in a 10 × 10 mm FOV. Measurements were made through the intact skull bone after opening the skin above. Baseline CBF was recorded for 5 min and hypercapnic challenge was induced by exposing animals to an air mixture containing 10% CO_2 for 2 min and for 2 min thereafter. CBF data (perfusion values, PU*sec, arbitrary unit) are presented as a percentage of baseline. Mice with incomplete LSCI protocol due to inappropriate length of anesthesia have been excluded from the analysis of hypercapnia measurements pre hoc.

In vivo two-photon imaging. C57BL/6 J, CX3CR1$^{GFP/+}$ and IL-1α$^{fl/flΔCX3CR1}$, were anaesthetized using 1,8% isoflurane and a 3 mm diameter cranial window was opened on the left hemisphere, above the primary somatosensory or the barrel cortex, without damaging the dura mater. After removal of the skull bone, a double circular glass coverslip was fixed with 3M™ Vetbond™. Above the dual coverslip, a custom-made metal headpiece (Femtonics Ltd., Budapest, Hungary) was fixed with dental cement. Three weeks after cranial window surgery, animals were treated with 3xLPS. 24 h after the 3rd LPS, animals were imaged under mild isoflurane (0,8-1%) anesthesia while the body temperature was maintained at 37 C°. Throughout the measurements, blood vessels were labeled with 100 μl (2 mg/ml in PBS) SR101 (#S359, Thermo Fisher) i.p., while leukocytes were labeled with 200 μl (1.4 mg/ml in saline) Rhodamine 6 G (#83697, Sigma) i.p. Two-photon imaging was performed with a Femto2D-DualScanhead microscope (Femtonics Ltd., Budapest, Hungary) coupled with a Chameleon Discovery laser (Coherent, Santa Clara, USA). The measurements were done with the 800 nm or 900 nm tunable wavelength laser excitation to simultaneously record SR101 and Rhodamine 6 G or CX3CR1$^{GFP/+}$ signals. For microglia-leukocyte interactions and leukocyte imaging in control animals, the resonant-scanning light path with 16x water-immersion objective (Nikon CFI75 LWD 16x W, NA 0.8) was used to acquire 30–40 min long recordings at 500 × 500 pixels resolution, at 30.958 Hz. Imaging was performed in superficial penetrating arteries (50–70 μm below the surface of the cerebral cortex), focusing on arterial segments after reaching the brain parenchyma. Data acquisition was performed by MESc software (v.3.5.6.9395SLE, Femtonics Ltd.).

EEG and parallel CBF measurements. EEG and Laser Doppler Flow recordings were conducted on the same set of animals as previously described[8]. EEG recordings were done in parallel with the hypercapnic challenge, allowing simultaneous assessment of neuronal activity and CBF. Briefly, animals were anesthetized with isoflurane (4% for induction, 0.6–0.9% for maintenance in the 2:1 mixture of N_2O andO_2,) and allowed to breathe spontaneously through a nose cone. The body temperature was maintained at 37 °C by using a heating pad equipped with a temperature probe and blanket feedback-controlled system (CODA Monitor, Kent Scientific Corporation). Mice were then fixed in the prone position in a stereotactic frame. A midline incision was made above the sagittal suture, and the skin was gently pulled aside. Surgical preparations were done under 1.5–2% isoflurane. EEG and laser-Doppler flow measurements were performed under mild isoflurane (0.1–0.3%) – medetomidine (initiation: i.p. 0.1 mg/kg, repeated 10 min later for maintenance) anesthesia. After 15-min baseline acquisition, a 2 min. hypercapnia was imposed by CO2-enriched gas inhalation (9.7% CO_2, 21% O_2 in N_2; Messer) at spontaneous respiration, which was repeated after a 5 min resting period, altogether 3 times. Single-

channel EEG and local CBF (by laser Doppler, PF4001 Master, Perimed AB, Järfälla, Sweden) were simultaneously monitored from the scalp of the parietal somatosensory cortex (stereotactic coordinates: -1 mm caudal and 4 mm lateral from Bregma). EEG was acquired through a silver ball electrode (EP1, World Precision Instruments, Sarasota, USA) connected to an AC-coupled head stage, pre-amplifier, amplifier modules (NL100AK, NL104A and NL106, NeuroLog System; Digitimer) and the associated signal conditioner (NL530, NeuroLog System; Digitimer). An Ag/AgCl electrode was implanted under the skin of the animal's neck to be used as reference electrode. The tips of the two probes (ball electrode and laser Doppler) were positioned as near as possible; the electrode contact gel also served as contact fluid for the laser Doppler probe. The recorded signals were then forwarded to an analog-to-digital converter (MP 150; Biopac Systems). Electrical signals were continuously acquired at a sampling frequency of 1 kHz using the software AcqKnowledge 4.2.0 (Biopac Systems). The laser-Doppler flow signal was digitized and displayed together with the EEG signal (MP 150 and AcqKnowledge 4.2.0; Biopac Systems). All analyses were performed offline by using the automated or inbuilt tools of the AcqKnowledge 4.2.0 software.

Quantification and statistical analysis. All statistical analysis were performed using Graphpad Prism 11.0.2 software (GraphPad Software, Inc). Sample size was determined by power calculation using G*Power 3.1.9.2 software before all experiments, with mean differences and 20-25% standard deviations based on pilot studies (power 80%, $\alpha = 0.05$). Data were assessed for normal distribution using the D'Agostino–Pearson normality test or the Shapiro–Wilk W test to determine the need for parametric or nonparametric analysis. For comparison of two groups, an unpaired *t*test with Welch's correction was used. For comparing more groups with parametric data, either one-way ANOVA or two-way ANOVA with Tukey's, Šídák's or Fisher's LSD multiple comparison tests were used. The most appropriate post-hoc test was chosen based on the recommendation by GraphPad Prism software, considering the number of comparisons made. For non-parametric data, Kruskal-Wallis test with Dunnett's multiple comparisons was used. For clarity of data presentation, non-significant (ns) results were omitted from the figures. Please refer to the figure legends and the results section for further details on statistical analysis. Data were presented as means ± SEM.

Reporting summary

Further information on research design is available in the Nature Portfolio Reporting Summary linked to this article.

Data availability

All data are included in this paper and supplementary information. Source data are provided with this paper. Additional information is available upon request. Source data are provided with this paper.

References

1. Van Hove, H., De Feo, D., Greter, M. & Becher, B. Central nervous system macrophages in health and disease. *Annu. Rev. Immunol.* **43**, 589–613 https://doi.org/10.1146/annurev-immunol-082423-041334 (2025).
2. Dalmau Gasull, A. et al. The niche matters: origin, function and fate of CNS-associated macrophages during health and disease. *Acta Neuropathol.* **147**, 37 https://doi.org/10.1007/s00401-023-02676-9 (2024).
3. Green, K. N., Crapser, J. D. & Hohsfield, L. A. To kill a microglia: a case for CSF1R inhibitors. *Trends Immunol.* **41**, 771–784 https://doi.org/10.1016/j.it.2020.07.001 (2020).
4. Bijnen, M., Sridhar, S., Keller, A. & Greter, M. Brain macrophages in vascular health and dysfunction. *Trends Immunol.* **46**, 46–60 https://doi.org/10.1016/j.it.2024.11.012 (2025).
5. Denes, A. et al. Endothelial cells and macrophages as allies in the healthy and diseased brain. *Acta Neuropathol.* **147**, 38 https://doi.org/10.1007/s00401-024-02695-0 (2024).
6. Prinz, M., Erny, D. & Hagemeyer, N. Ontogeny and homeostasis of CNS myeloid cells. *Nat. Immunol.* **18**, 385–392 https://doi.org/10.1038/ni.3703 (2017).
7. Bisht, K. et al. Capillary-associated microglia regulate vascular structure and function through PANX1-P2RY12 coupling in mice. *Nat. Commun.* **12**, 5289 https://doi.org/10.1038/s41467-021-25590-8 (2021).
8. Császár, E. et al. Microglia modulate blood flow, neurovascular coupling, and hypoperfusion via purinergic actions. *J. Exp. Med.* **219** https://doi.org/10.1084/jem.20211071 (2022).
9. Mondo, E. et al. A developmental analysis of juxtavascular microglia dynamics and interactions with the vasculature. *J. Neurosci.* **40**, 6503–6521 https://doi.org/10.1523/jneurosci.3006-19.2020 (2020).
10. Dudvarski Stankovic, N., Teodorczyk, M., Ploen, R., Zipp, F. & Schmidt, M. H. H. Microglia-blood vessel interactions: a double-edged sword in brain pathologies. *Acta Neuropathol.* **131**, 347–363 https://doi.org/10.1007/s00401-015-1524-y (2016).
11. Li, Q. et al. Developmental heterogeneity of microglia and brain myeloid cells revealed by deep single-cell RNA sequencing. *Neuron* **101**, 207–223.e210 https://doi.org/10.1016/j.neuron.2018.12.006 (2019).
12. Hattori, Y. The microglia-blood vessel interactions in the developing brain. *Neurosci. Res.* **187**, 58–66 https://doi.org/10.1016/j.neures.2022.09.006 (2023).
13. Zhao, X. L., Eyo, U. B., Murugan, M. & Wu, L. J. Microglial interactions with the neurovascular system in physiology and pathology. *Dev. Neurobiol.* **78**, 604–617 https://doi.org/10.1002/dneu.22576 (2018).
14. Masuda, T., Croom, D., Hida, H. & Kirov, S. A. Capillary blood flow around microglial somata determines dynamics of microglial processes in ischemic conditions. *Glia*. **59**, 1744–1753 https://doi.org/10.1002/glia.21220 (2011).
15. Fekete, R. et al. Microglia control the spread of neurotropic virus infection via P2Y12 signalling and recruit monocytes through P2Y12-independent mechanisms. *Acta Neuropathol.* **136**, 461–482 https://doi.org/10.1007/s00401-018-1885-0 (2018).
16. Otxoa-de-Amezaga, A. et al. Microglial cell loss after ischemic stroke favors brain neutrophil accumulation. *Acta Neuropathol.* **137**, 321–341 https://doi.org/10.1007/s00401-018-1954-4 (2019).
17. Wendeln, A. C. et al. Innate immune memory in the brain shapes neurological disease hallmarks. *Nature* **556**, 332–338 https://doi.org/10.1038/s41586-018-0023-4 (2018).
18. Haruwaka, K. et al. Dual microglia effects on blood brain barrier permeability induced by systemic inflammation. *Nat. Commun.* **10**, 5816 https://doi.org/10.1038/s41467-019-13812-z (2019).
19. Drake, C. et al. Brain inflammation is induced by co-morbidities and risk factors for stroke. *Brain Behav. Immun.* **25**, 1113–1122 https://doi.org/10.1016/j.bbi.2011.02.008 (2011).
20. Hoogland, I. C. M., Houbolt, C., van Westerloo, D. J., van Gool, W. A. & van de Beek, D. Systemic inflammation and microglial activation: systematic review of animal experiments. *J. Neuroinflamm.* **12** https://doi.org/10.1186/s12974-015-0332-6 (2015).
21. Iadecola, C. The neurovascular unit coming of age: a journey through neurovascular coupling in health and disease. *Neuron* **96**, 17–42 https://doi.org/10.1016/j.neuron.2017.07.030 (2017).
22. Korte, N., Nortley, R. & Attwell, D. Cerebral blood flow decrease as an early pathological mechanism in Alzheimer's disease. *Acta Neuropathologica* **140**, 793–810 https://doi.org/10.1007/s00401-020-02215-w (2020).

23. Rauchmann, B. S. et al. Microglial activation and connectivity in alzheimer disease and aging. *Ann. Neurol.* **92**, 768–781 https://doi.org/10.1002/ana.26465 (2022).
24. van Dinther, M. et al. Lower cerebral blood flow predicts cognitive decline in patients with vascular cognitive impairment. *Alzheimers Dement* **20**, 136–144 https://doi.org/10.1002/alz.13408 (2024).
25. Nayak, D., Roth, T. L. & McGavern, D. B. Microglia development and function. *Annu. Rev. Immunol.* **32**, 367–402 https://doi.org/10.1146/annurev-immunol-032713-120240 (2014).
26. Dinarello, C. A. Immunological and inflammatory functions of the interleukin-1 family. *Annu. Rev. Immunol.* **27**, 519–550 https://doi.org/10.1146/annurev.immunol.021908.132612 (2009).
27. Gibson, R. M., Rothwell, N. J. & Le Feuvre, R. A. CNS injury: the role of the cytokine IL-1. *Vet. J.* **168**, 230–237 https://doi.org/10.1016/j.tvjl.2003.10.016 (2004).
28. Shaftel, S. S. et al. Chronic interleukin-1beta expression in mouse brain leads to leukocyte infiltration and neutrophil-independent blood brain barrier permeability without overt neurodegeneration. *J. Neurosci.* **27**, 9301–9309 https://doi.org/10.1523/jneurosci.1418-07.2007 (2007).
29. Shaftel, S. S., Griffin, W. S. & O'Banion, M. K. The role of interleukin-1 in neuroinflammation and Alzheimer disease: an evolving perspective. *J. Neuroinflammation* **5**, 7 https://doi.org/10.1186/1742-2094-5-7 (2008).
30. Sienel, R. I., Kataoka, H., Kim, S. W., Seker, F. B. & Plesnila, N. Adhesion of leukocytes to cerebral venules precedes neuronal cell death and is sufficient to trigger tissue damage after cerebral ischemia. *Front Neurol.* **12**, 807658 https://doi.org/10.3389/fneur.2021.807658 (2021).
31. Ching, S. et al. Endothelial-specific knockdown of interleukin-1 (IL-1) type 1 receptor differentially alters CNS responses to IL-1 depending on its route of administration. *J. Neurosci.* **27**, 10476–10486 https://doi.org/10.1523/jneurosci.3357-07.2007 (2007).
32. Giles, J. A. et al. Requirement for interleukin-1 to drive brain inflammation reveals tissue-specific mechanisms of innate immunity. *Eur. J. Immunol.* **45**, 525–530 https://doi.org/10.1002/eji.201444748 (2015).
33. Berchtold, D., Priller, J., Meisel, C. & Meisel, A. Interaction of microglia with infiltrating immune cells in the different phases of stroke. *Brain Pathol.* **30**, 1209–1219 https://doi.org/10.1111/bpa.12911 (2020).
34. Kim, Y. R. et al. Neutrophils return to bloodstream through the brain blood vessel after crosstalk with microglia during LPS-induced neuroinflammation. *Front. Cell Dev. Biol.* **8** https://doi.org/10.3389/fcell.2020.613733 (2020).
35. Dantzer, R., O'Connor, J. C., Freund, G. G., Johnson, R. W. & Kelley, K. W. From inflammation to sickness and depression: when the immune system subjugates the brain. *Nat. Rev. Neurosci.* **9**, 46–56 https://doi.org/10.1038/nrn2297 (2008).
36. Herber, D. L. et al. Diverse microglial responses after intrahippocampal administration of lipopolysaccharide. *Glia* **53**, 382–391 https://doi.org/10.1002/glia.20272 (2006).
37. Proescholdt, M. G. et al. Intracerebroventricular but not intravenous interleukin-1beta induces widespread vascular-mediated leukocyte infiltration and immune signal mRNA expression followed by brain-wide glial activation. *Neuroscience* **112**, 731–749 https://doi.org/10.1016/s0306-4522(02)00048-9 (2002).
38. Faraco, G. et al. Perivascular macrophages mediate the neurovascular and cognitive dysfunction associated with hypertension. *J. Clin. Investig.* **126**, 4674–4689 https://doi.org/10.1172/JCI86950 (2016).
39. Goldmann, T. et al. Origin, fate and dynamics of macrophages at central nervous system interfaces. *Nat. Immunol.* **17**, 797 https://doi.org/10.1038/ni.3423 (2016).
40. Mrdjen, D. et al. High-dimensional single-cell mapping of central nervous system immune cells reveals distinct myeloid subsets in health, aging, and disease (vol 48, pg 380, 2018). *Immunity* **48**, 599–599 https://doi.org/10.1016/j.immuni.2018.02.014 (2018).
41. Hallmann, R. et al. Expression and function of laminins in the embryonic and mature vasculature. *Physiol. Rev.* **85**, 979–1000 https://doi.org/10.1152/physrev.00014.2004 (2005).
42. Yousif, L. F., Di Russo, J. & Sorokin, L. Laminin isoforms in endothelial and perivascular basement membranes. *Cell Adh Migr.* **7**, 101–110 https://doi.org/10.4161/cam.22680 (2013).
43. Di Russo, J. et al. Vascular laminins in physiology and pathology. *Matrix Biol.* **57-58**, 140–148 https://doi.org/10.1016/j.matbio.2016.06.008 (2017).
44. Hannocks, M. J. et al. Molecular characterization of perivascular drainage pathways in the murine brain. *J. Cereb. Blood Flow. Metab.* **38**, 669–686 https://doi.org/10.1177/0271678x17749689 (2018).
45. Owens, T., Bechmann, I. & Engelhardt, B. Perivascular spaces and the two steps to neuroinflammation. *J. Neuropathol. Exp. Neurol.* **67**, 1113–1121 https://doi.org/10.1097/NEN.0b013e31818f9ca8 (2008).
46. Mun, K. T. & Hinman, J. D. Inflammation and the link to vascular brain health: timing is brain. *Stroke* **53**, 427–436 https://doi.org/10.1161/Strokeaha.121.032613 (2022).
47. Fruekilde, S. K. et al. Disturbed microcirculation and hyperaemic response in a murine model of systemic inflammation. *J. Cerebr Blood F. Met.* **42**, 2303–2317 https://doi.org/10.1177/0271678x221112278 (2022).
48. Montagne, A. et al. Ultra-sensitive molecular MRI of cerebrovascular cell activation enables early detection of chronic central nervous system disorders. *Neuroimage* **63**, 760–770 https://doi.org/10.1016/j.neuroimage.2012.07.018 (2012).
49. McAteer, M. A. et al. In vivo magnetic resonance imaging of acute brain inflammation using microparticles of iron oxide. *Nat. Med.* **13**, 1253–1258 https://doi.org/10.1038/nm1631 (2007).
50. Kodali, M. C., Chen, H. & Liao, F. F. Temporal unsnarling of brain's acute neuroinflammatory transcriptional profiles reveals panendothelitis as the earliest event preceding microgliosis. *Mol. Psychiatry* **26**, 3905–3919 https://doi.org/10.1038/s41380-020-00955-5 (2021).
51. Hamzic, N., Blomqvist, A. & Nilsberth, C. Immune-induced expression of lipocalin-2 in brain endothelial cells: relationship with interleukin-6, cyclooxygenase-2 and the febrile response. *J. Neuroendocrinol.* **25**, 271–280 https://doi.org/10.1111/jne.12000 (2013).
52. Yoon, S. H. et al. Microglial NLRP3-gasdermin D activation impairs blood-brain barrier integrity through interleukin-1β-independent neutrophil chemotaxis upon peripheral inflammation in mice. *Nat. Commun.* **16** https://doi.org/10.1038/s41467-025-56097-1 (2025).
53. Wong, R. et al. Interleukin-1 mediates ischaemic brain injury via distinct actions on endothelial cells and cholinergic neurons. *Brain Behav. Immun.* **76**, 126–138 https://doi.org/10.1016/j.bbi.2018.11.012 (2019).
54. Thornton, P. D. & Heise, A. Highly specific dual enzyme-mediated payload release from peptide-coated silica particles. *J. Am. Chem. Soc.* **132**, 2024–2028 https://doi.org/10.1021/ja9094439 (2010).
55. Allen, C. et al. Neutrophil cerebrovascular transmigration triggers rapid neurotoxicity through release of proteases associated with decondensed DNA. *J. Immunol.* **189**, 381–392 https://doi.org/10.4049/jimmunol.1200409 (2012).
56. Liu, X. et al. Cell-type-specific interleukin 1 receptor 1 signaling in the brain regulates distinct neuroimmune activities. *Immunity* **50**, 317–333.e316 https://doi.org/10.1016/j.immuni.2018.12.012 (2019).

57. Rajkowska, G., Hughes, J., Stockmeier, C. A., Miguel-Hidalgo, J. J. & Maciag, D. Coverage of blood vessels by astrocytic endfeet is reduced in major depressive disorder. *Biol. Psychiat* **73**, 613–621 https://doi.org/10.1016/j.biopsych.2012.09.024 (2013).
58. Niu, J. Q. et al. Aberrant oligodendroglial-vascular interactions disrupt the blood-brain barrier, triggering CNS inflammation. *Nat. Neurosci.* **22**, 709 https://doi.org/10.1038/s41593-019-0369-4 (2019).
59. Steiner, E. et al. Loss of astrocyte polarization upon transient focal brain ischemia as a possible mechanism to counteract early edema formation. *Glia* **60**, 1646–1659 https://doi.org/10.1002/glia.22383 (2012).
60. Denes, A. et al. Proliferating resident microglia after focal cerebral ischaemia in mice. *J. Cereb. Blood Flow. Metab.* **27**, 1941–1953 https://doi.org/10.1038/sj.jcbfm.9600495 (2007).
61. Dénes, A., Ferenczi, S., Halász, J., Környei, Z. & Kovács, K. J. Role of CX3CR1 (fractalkine receptor) in brain damage and inflammation induced by focal cerebral ischemia in mouse. *J. Cereb. Blood Flow. Metab.* **28**, 1707–1721 https://doi.org/10.1038/jcbfm.2008.64 (2008).
62. Spangenberg, E. et al. Sustained microglial depletion with CSF1R inhibitor impairs parenchymal plaque development in an Alzheimer's disease model. *Nat. Commun.* **10**, 3758 https://doi.org/10.1038/s41467-019-11674-z (2019).
63. Szalay, G. et al. Microglia protect against brain injury and their selective elimination dysregulates neuronal network activity after stroke. *Nat. Commun.* **7** https://doi.org/10.1038/ncomms11499 (2016).
64. Drieu, A. et al. Alcohol exposure-induced neurovascular inflammatory priming impacts ischemic stroke and is linked with brain perivascular macrophages. *JCI Insight* **5** https://doi.org/10.1172/jci.insight.129226 (2020).
65. Levard, D. et al. Central nervous system-associated macrophages modulate the immune response following stroke in aged mice. *Nat. Neurosci.* **27** https://doi.org/10.1038/s41593-024-01695-3 (2024).
66. Culemann, S. et al. Addendum: stunning of neutrophils accounts for the anti-inflammatory effects of clodronate liposomes. *J. Exp. Med.* **220** https://doi.org/10.1084/jem.20220525060220023a (2023).
67. Drieu, A. et al. Parenchymal border macrophages regulate the flow dynamics of the cerebrospinal fluid. *Nature* **611**, 585 https://doi.org/10.1038/s41586-022-05397-3 (2022).
68. Audoy-Remus, J. et al. Rod-Shaped monocytes patrol the brain vasculature and give rise to perivascular macrophages under the influence of proinflammatory cytokines and angiopoietin-2. *J. Neurosci.* **28**, 10187–10199 https://doi.org/10.1523/JNEUROSCI.3510-08.2008 (2008).
69. Jordão, M. J. C. et al. Single-cell profiling identifies myeloid cell subsets with distinct fates during neuroinflammation. *Science* **363** https://doi.org/10.1126/science.aat7554 (2019).
70. Rojo, R. et al. Deletion of a Csf1r enhancer selectively impacts CSF1R expression and development of tissue macrophage populations. *Nat. Commun.* **10**, 3215 https://doi.org/10.1038/s41467-019-11053-8 (2019).
71. Munro, D. A. D. et al. CNS macrophages differentially rely on an intronic Csf1r enhancer for their development. *Development* **147** https://doi.org/10.1242/dev.194449 (2020).
72. Li, Q. M. et al. Endothelial IL-1R1 is a critical mediator of EAE pathogenesis. *Brain Behav. Immun.* **25**, 160–167 https://doi.org/10.1016/j.bbi.2010.09.009 (2011).
73. Bevilacqua, M. P. et al. Interleukin-1 activation of vascular endothelium. Effects on procoagulant activity and leukocyte adhesion. *Am. J. Pathol.* **121**, 394–403 (1985).
74. Luis, J. P., Simoes, C. J. V. & Brito, R. M. M. The therapeutic prospects of targeting IL-1R1 for the modulation of neuroinflammation in central nervous system disorders. *Int. J. Mol. Sci.* **23** https://doi.org/10.3390/ijms23031731 (2022).
75. Freria, C. M. et al. Serial systemic injections of endotoxin (LPS) elicit neuroprotective spinal cord microglia through IL-1-dependent cross talk with endothelial cells. *J. Neurosci.* **40**, 9103–9120 https://doi.org/10.1523/jneurosci.0131-20.2020 (2020).
76. Heindl, S. et al. Automated morphological analysis of microglia after stroke. *Front. Cell Neurosci.* **12**, 106 https://doi.org/10.3389/fncel.2018.00106 (2018).
77. Nemeth, D. P. et al. Dynamic interleukin-1 receptor type 1 signaling mediates microglia-vasculature interactions following repeated systemic LPS. *J. Inflamm. Res.* **15**, 1575–1590 https://doi.org/10.2147/JIR.S350114 (2022).
78. You, Y. et al. Cell-specific IL-1R1 regulates the regional heterogeneity of microglial displacement of GABAergic synapses and motor learning ability. *Cell Mol. Life Sci.* **81**, 116 https://doi.org/10.1007/s00018-023-05111-0 (2024).
79. Konsman, J. P., Vigues, S., Mackerlova, L., Bristow, A. & Blomqvist, A. Rat brain vascular distribution of interleukin-1 type-1 receptor immunoreactivity: relationship to patterns of inducible cyclooxygenase expression by peripheral inflammatory stimuli. *J. Comp. Neurol.* **472**, 113–129 https://doi.org/10.1002/cne.20052 (2004).
80. Rajeev, V. et al. Chronic cerebral hypoperfusion: a critical feature in unravelling the etiology of vascular cognitive impairment. *Acta Neuropathol. Commun.* **11**, 93 https://doi.org/10.1186/s40478-023-01590-1 (2023).
81. Naveed, M., Zhou, Q. G. & Han, F. Cerebrovascular inflammation: a critical trigger for neurovascular injury? *Neurochem. Int.* **126**, 165–177 https://doi.org/10.1016/j.neuint.2019.03.011 (2019).
82. Tian, Z. M., Ji, X. M. & Liu, J. Neuroinflammation in vascular cognitive impairment and dementia: current evidence, advances, and prospects. *Int. J. Mol. Sci.* **23** https://doi.org/10.3390/ijms23116224 (2022).
83. Yoon, S., Zuccarello, M. & Rapoport, R. M. pCO(2) and pH regulation of cerebral blood flow. *Front. Physiol.* **3**, 365 https://doi.org/10.3389/fphys.2012.00365 (2012).
84. Hoiland, R. L., Fisher, J. A. & Ainslie, P. N. Regulation of the cerebral circulation by arterial carbon dioxide. *Compr. Physiol.* **9**, 1101–1154 https://doi.org/10.1002/cphy.c180021 (2019).
85. Meng, L. & Gelb, A. W. Regulation of cerebral autoregulation by carbon dioxide. *Anesthesiology* **122**, 196–205 https://doi.org/10.1097/aln.0000000000000506 (2015).
86. Fu, Z. X. et al. Microglia modulate the cerebrovascular reactivity through ectonucleotidase CD39. *Nat. Commun.* **16** https://doi.org/10.1038/s41467-025-56093-5 (2025).
87. Kolaczkowska, E. & Kubes, P. Neutrophil recruitment and function in health and inflammation. *Nat. Rev. Immunol.* **13**, 159–175 https://doi.org/10.1038/nri3399 (2013).
88. Reichenbach, Z. W., Li, H., Gaughan, J. P., Elliott, M. & Tuma, R. IV and IP administration of rhodamine in visualization of WBC-BBB interactions in cerebral vessels. *Microsc. Res. Tech.* **78**, 894–899 https://doi.org/10.1002/jemt.22552 (2015).
89. Hülsmann, S., Hagos, L., Heuer, H. & Schnell, C. Limitations of Sulforhodamine 101 for Brain Imaging. *Front. Cell Neurosci.* **11**, 44 https://doi.org/10.3389/fncel.2017.00044 (2017).
90. Masamoto, K. et al. Repeated longitudinal imaging of neuro-glio-vascular unit at the peripheral boundary of ischemia in mouse cerebral cortex. *Neuroscience* **212**, 190–200 https://doi.org/10.1016/j.neuroscience.2012.03.034 (2012).
91. Li, H. et al. In vivo identification of arteries and veins using two-photon excitation elastin autofluorescence. *J. Anat.* **236**, 171–179 https://doi.org/10.1111/joa.13080 (2020).

92. Simmons, S. B., Liggitt, D. & Goverman, J. M. Cytokine-regulated neutrophil recruitment is required for brain but not spinal cord inflammation during experimental autoimmune encephalomyelitis. *J. Immunol.* **193**, 555–563 https://doi.org/10.4049/jimmunol.1400807 (2014).
93. Agrawal, S. et al. Dystroglycan is selectively cleaved at the parenchymal basement membrane at sites of leukocyte extravasation in experimental autoimmune encephalomyelitis. *J. Exp. Med.* **203**, 1007–1019 https://doi.org/10.1084/jem.20051342 (2006).
94. Perez-de-Puig, I. et al. Neutrophil recruitment to the brain in mouse and human ischemic stroke. *Acta Neuropathol.* **129**, 239–257 https://doi.org/10.1007/s00401-014-1381-0 (2015).
95. Corps, K. N., Roth, T. L. & McGavern, D. B. Inflammation and neuroprotection in traumatic brain injury. *JAMA Neurol.* **72**, 355–362 https://doi.org/10.1001/jamaneurol.2014.3558 (2015).
96. Faraco, G., Park, L., Anrather, J. & Iadecola, C. Brain perivascular macrophages: characterization and functional roles in health and disease. *J. Mol. Med.* **95**, 1143–1152 https://doi.org/10.1007/s00109-017-1573-x (2017).
97. Goddery, E. N. et al. Microglia and perivascular macrophages act as antigen presenting cells to promote CD8 T cell infiltration of the brain. *Front. Immunol.* **12** https://doi.org/10.3389/fimmu.2021.726421 (2021).
98. Polfliet, M. M. J., *et al*. Meningeal and perivascular macrophages of the central nervous system play a protective role during bacterial meningitis. *Journal of Immunology* **167**, 4644-4650 https://doi.org/10.4049/jimmunol.167.8.4644 (2001).
99. Hedrick, C. C. & Malanchi, I. Neutrophils in cancer: heterogeneous and multifaceted. *Nat. Rev. Immunol.* **22**, 173–187 https://doi.org/10.1038/s41577-021-00571-6 (2022).
100. D'Mello, C., Le, T. & Swain, M. G. Cerebral microglia recruit monocytes into the brain in response to tumor necrosis factorα signaling during peripheral organ inflammation. *J. Neurosci.* **29**, 2089–2102 https://doi.org/10.1523/Jneurosci.3567-08.2009 (2009).
101. McColl, B. W., Rothwell, N. J. & Allan, S. M. Systemic inflammatory stimulus potentiates the acute phase and CXC chemokine responses to experimental stroke and exacerbates brain damage via interleukin-1- and neutrophil-dependent mechanisms. *J. Neurosci.* **27**, 4403–4412 https://doi.org/10.1523/JNEUROSCI.5376-06.2007 (2007).
102. Dénes, A. et al. Streptococcus pneumoniae worsens cerebral ischemia via interleukin 1 and platelet glycoprotein Ibα. *Ann. Neurol.* **75**, 670–683 https://doi.org/10.1002/ana.24146 (2014).
103. Rossi, B., Santos-Lima, B., Terrabuio, E., Zenaro, E. & Constantin, G. Common peripheral immunity mechanisms in multiple sclerosis and Alzheimer's disease. *Front. Immunol.* **12** https://doi.org/10.3389/fimmu.2021.639369 (2021).
104. Lapenna, A., De Palma, M. & Lewis, C. E. Perivascular macrophages in health and disease. *Nat. Rev. Immunol.* **18**, 689–702 https://doi.org/10.1038/s41577-018-0056-9 (2018).
105. Kurz, C., Walker, L., Rauchmann, B. S. & Perneczky, R. Dysfunction of the blood-brain barrier in Alzheimer's disease: evidence from human studies. *Neuropathol. Appl Neurobiol.* **48**, e12782 https://doi.org/10.1111/nan.12782 (2022).
106. Qin, J. et al. Perivascular macrophages create an intravascular niche for CD8(+) T cell localisation prior to the onset of fatal experimental cerebral malaria. *Clin. Transl. Immunol.* **10**, e1273 https://doi.org/10.1002/cti2.1273 (2021).
107. Park, L. et al. Brain perivascular macrophages initiate the neurovascular dysfunction of Alzheimer Aβ peptides. *Circ. Res.* **121**, 258–269 https://doi.org/10.1161/circresaha.117.311054 (2017).
108. Iyonaga, T., Shinohara, K., Mastuura, T., Hirooka, Y. & Tsutsui, H. Brain perivascular macrophages contribute to the development of hypertension in stroke-prone spontaneously hypertensive rats via sympathetic activation. *Hypertens. Res.* **43**, 99–110 https://doi.org/10.1038/s41440-019-0333-4 (2020).
109. Santisteban, M. M. et al. Endothelium-macrophage crosstalk mediates blood-brain barrier dysfunction in hypertension. *Hypertension* **76**, 795–807 https://doi.org/10.1161/hypertensionaha.120.15581 (2020).
110. Pires, P. W. et al. Improvement in middle cerebral artery structure and endothelial function in stroke-prone spontaneously hypertensive rats after macrophage depletion. *Microcirculation* **20**, 650–661 https://doi.org/10.1111/micc.12064 (2013).
111. Pedragosa, J. et al. CNS-border associated macrophages respond to acute ischemic stroke attracting granulocytes and promoting vascular leakage. *Acta Neuropathol. Commun.* **6**, 76 https://doi.org/10.1186/s40478-018-0581-6 (2018).
112. Polfliet, M. M. et al. Meningeal and perivascular macrophages of the central nervous system play a protective role during bacterial meningitis. *J. Immunol.* **167**, 4644–4650 https://doi.org/10.4049/jimmunol.167.8.4644 (2001).
113. Goddery, E. N. et al. Microglia and perivascular macrophages act as antigen presenting cells to promote CD8 T cell infiltration of the brain. *Front. Immunol.* **12**, 726421 https://doi.org/10.3389/fimmu.2021.726421 (2021).
114. Hammond, T. R. et al. Single-cell RNA sequencing of microglia throughout the mouse lifespan and in the injured brain reveals complex cell-state changes. *Immunity* **50**, 253 https://doi.org/10.1016/j.immuni.2018.11.004 (2019).
115. Marschallinger, J. et al. Lipid-droplet-accumulating microglia represent a dysfunctional and proinflammatory state in the aging brain. *Nat. Neurosci.* **23**, 194 https://doi.org/10.1038/s41593-019-0566-1 (2020).
116. Silvin, A. et al. Dual ontogeny of disease-associated microglia and disease inflammatory macrophages in aging and neurodegeneration. *Immunity* **55**, 1448 https://doi.org/10.1016/j.immuni.2022.07.004 (2022).
117. He, H. et al. NK cells promote neutrophil recruitment in the brain during sepsis-induced neuroinflammation. *Sci Rep-Uk* **6** https://doi.org/10.1038/srep27711 (2016).
118. Thomson, C. A., McColl, A., Graham, G. J. & Cavanagh, J. Sustained exposure to systemic endotoxin triggers chemokine induction in the brain followed by a rapid influx of leukocytes. *J. Neuroinflamm.* **17** https://doi.org/10.1186/s12974-020-01759-8 (2020).
119. Zhou, H., Andonegui, G., Wong, C. H. Y. & Kubes, P. Role of endothelial TLR4 for neutrophil recruitment into central nervous system microvessels in systemic inflammation. *J. Immunol.* **183**, 5244–5250 https://doi.org/10.4049/jimmunol.0901309 (2009).
120. Zhou, H., Lapointe, B. M., Clark, S. R., Zbytnuik, L. & Kubes, P. A requirement for microglial TLR4 in leukocyte recruitment into brain in response to lipopolysaccharide. *J. Immunol.* **177**, 8103–8110 https://doi.org/10.4049/jimmunol.177.11.8103 (2006).
121. Bowyer, J. F. et al. Microglial activation and responses to vasculature that result from an acute LPS exposure. *Neurotoxicology* **77**, 181–192 https://doi.org/10.1016/j.neuro.2020.01.014 (2020).
122. Tsioti, I. et al. Endothelial Toll-like receptor 4 is required for microglia activation in the murine retina after systemic lipopolysaccharide exposure. *J Neuroinflamm* **20** https://doi.org/10.1186/s12974-023-02712-1 (2023).
123. Xingi, E. et al. LPS-induced systemic inflammation affects the dynamic interactions of astrocytes and microglia with the

vasculature of the mouse brain cortex. *Cells-Basel* **12** https://doi.org/10.3390/cells12101418 (2023).
124. Gölöncsér, F. et al. Involvement of P2Y12 receptors in a nitroglycerin-induced model of migraine in male mice. *Brit J. Pharm.* **178**, 4626–4645 https://doi.org/10.1111/bph.15641 (2021).
125. Abdulaal, W. H. et al. Characterization of a conditional interleukin-1 receptor 1 mouse mutant using the Cre/LoxP system. *Eur. J. Immunol.* **46**, 912–918 https://doi.org/10.1002/eji.201546075 (2016).
126. Gothert, J. R. et al. Genetically tagging endothelial cells in vivo: bone marrow-derived cells do not contribute to tumor endothelium. *Blood* **104**, 1769–1777 https://doi.org/10.1182/blood-2003-11-3952 (2004).
127. Bageghni, S. A. et al. Fibroblast-specific deletion of interleukin-1 receptor-1 reduces adverse cardiac remodeling following myocardial infarction. *JCI Insight* **5** https://doi.org/10.1172/jci.insight.125074 (2019).
128. Helyes, Z. et al. Transfer of complex regional pain syndrome to mice via human autoantibodies is mediated by interleukin-1-induced mechanisms. *Proc. Natl. Acad. Sci. USA* **116**, 13067–13076 https://doi.org/10.1073/pnas.1820168116 (2019).
129. Gauberti, M., Fournier, A. P., Docagne, F., Vivien, D. & Martinez de Lizarrondo, S. Molecular Magnetic Resonance Imaging of Endothelial Activation in the Central Nervous System. *Theranostics* **8**, 1195–1212 https://doi.org/10.7150/thno.22662 (2018).
130. Yushkevich, P. A. et al. User-guided 3D active contour segmentation of anatomical structures: significantly improved efficiency and reliability. *Neuroimage* **31**, 1116–1128 https://doi.org/10.1016/j.neuroimage.2006.01.015 (2006).
131. Mastronarde, D. N. Automated electron microscope tomography using robust prediction of specimen movements. *J. Struct. Biol.* **152**, 36–51 https://doi.org/10.1016/j.jsb.2005.07.007 (2005).
132. Kremer, J. R., Mastronarde, D. N. & McIntosh, J. R. Computer visualization of three-dimensional image data using IMOD. *J. Struct. Biol.* **116**, 71–76 https://doi.org/10.1006/jsbi.1996.0013 (1996).

Acknowledgements

The authors thank Pál Vági of the Light Microscopy Center at the HUN-REN Institute of Experimental Medicine, Hungary for kindly providing microscopy support. We also thank the Medical Gene Technology Unit and the Cell Biology Center at the HUN-REN Institute of Experimental Medicine for their support. The authors are grateful to Plexxikon for providing PLX5622 for these studies. The authors are grateful to Clare Pridans for providing us with the CSF1R$^{\Delta FIRE/\Delta FIRE}$ mice.

Author contributions

A.R.B. and N.L, designed, conducted the experiments and analyzed the data; A.R.B. performed flow cytometry, immunohistochemistry confocal microscopy and histological quantifications; N.L. preformed Laser Speckle Contrast and in vivo two photon imaging, flow cytometry and data analysis. A.R.B., M.R., M.G., and D.L. conducted MRI and analyzed the data. M.R. and D.L. performed flow cytometry of clodronate treated animals. Á.M. conducted EEG and LDF measurements and provided intellectual support. C.C. designed anatomic experiments and performed electron microscopy and Stimulated Emission Depletion (STED) microscopy and analyzed microscopy data. B.P. adapted automated microglia analysis set up. E.C. analyzed two-photon data. S.K.R. Samawar contributed data interpretation. L.S. kindly provided laminin antibodies and essential intellectual support. C.P. provided CSF1R$^{\Delta FIRE/\Delta FIRE}$ mice, methodological and conceptual support, and edited the manuscript. E.F. and D.V. provided overall supervision and intellectual support. E.F. contributed to obtain funding. A.D. devised the study, designed the experiments, provided overall supervision for the project and obtained funding. The manuscript was written by A.R.B., N.L., and A.D. with input from all authors.

Funding

This work was supported with funding from the ERC-CoG 724994 (A. Denes), the "Momentum" Program of the Hungarian Academy of Sciences (LP2016- 4/2016 to A. Denes) and the Hungarian Brain Research Program KTIA_13_NAP-A-I/ 2(A. Denes). This project has also received funding from the European Union's Horizon 2020 research and innovation program under the Marie Skłodowska-Curie grant "ENTRAIN" agreement no. 813294 (A.R. Brás and A. Denes). L. Sorokin was supported by the ERC-2021-ADG 101054805 - B3MN. D. Vivien, M. Rubio and A. Denes were supported by the ERA-NET 2024 MeniSPYs. Á. Menyhárt was supported by grants from the National Research, Development and Innovation Office of Hungary (NKFIH STARTING_24 (No. 150356) and FK142218). E. Farkas was supported by National Research, Development and Innovation Office of Hungary, K146725. N. Lénárt, C. Cserép, B. Pósfai, Á. Menyhárt were supported by the János Bolyai Research Scholarship of the Hungarian Academy of Sciences. N. Lénárt was supported by the UNKP-21-5 New National Excellence Program of the Ministry for Innovation and Technology from the source of the National Research, Development and Innovation Fund. B. Pósfai was supported by the EKÖP-2025-433 University Research Scholarship Program of the Ministry of Culture and Innovation from the source of the National Research, Development and Innovation Fund.

Competing interests

The authors declare no competing interests.

Additional information

Supplementary information The online version contains supplementary material available at https://doi.org/10.1038/s41467-026-77787-4.

Correspondence and requests for materials should be addressed to Ádám. Dénes.

Peer review information *Nature Communications* thanks the anonymous reviewers for their contribution to the peer review of this work. A peer review file is available.

This Article in Press is shared early to give you faster access to new research. It is citable and carries a permanent DOI. The final edited version will replace it automatically.

[1]"Momentum" Laboratory of Neuroimmunology, HUN-REN Institute of Experimental Medicine, Budapest, Hungary. [2]János Szentágothai Doctoral School of Neurosciences, Schools of PhD Studies, Semmelweis University, Budapest, Hungary. [3]Normandie University, Caen Normandie University, UNICAEN, INSERM U1237, Physiopathology and Imaging of Neurological Disorders (PhIND), Cyceron, Institut Blood and Brain @ Caen-Normandie (BB@C), Caen, France. [4]Hungarian Centre of Excellence for Molecular Medicine – University of Szeged, Cerebral Blood Flow and Metabolism Research Group, Szeged, Hungary. [5]Department of Cell Biology and Molecular Medicine, Albert Szent-Györgyi Medical School and Faculty of Science and Informatics, University of Szeged, Szeged, Hungary. [6]Institute of Physiological Chemistry and Pathobiochemistry, University of Muenster, Munster, Germany. [7]Cells-in-Motion Interfaculty Centre (CIMIC), University of Münster, Münster, Germany. [8]Centre for Inflammation Research Institute for Regeneration and Repair, University of Edinburgh, Edinburgh, UK. [9]Department of Clinical Research, Caen University Hospital, Caen, France. [10]Present address: Department of Neuroscience, Yale School of Medicine, Yale University, 333 Cedar Street, New Haven, CT, USA. [11]These authors contributed equally: Ana Rita Brás, Nikolett Lénárt. denes.adam@koki.hun-ren.hu